Site Specific Relaxation Dynamics of Luminescent Centers

by

Deegala Dorage Mayuri Perera

(Under the direction of Uwe Happek)

Abstract

The relaxation dynamics of Ce^{3+} ions in phosphor materials relevant to solid state lighting has been investigated. Of particular interest was the temperature dependence of the emission efficiency in heavily doped yttrium aluminum garnet (YAG) materials, which show a decreased quenching temperature compared to low concentration samples. Using site selective spectroscopy, we demonstrate that the lowering of the quenching temperature in high concentration samples is due to cerium ions in distorted sites. Our results can be generalized that high concentrations of cerium and/or an addition of optically mute rare earth ions to broaden the emission spectrum will lead to a lowered quenching temperature. We studied also $Na_2Gd_2O(BO_3)_2$ doped with Ce^{3+}, a system where Ce^{3+} ions occupy two distinct lattice sites. In this case it is shown that the luminescence quenching is due to photoionization.

Index words: Lifetime Measurements, Luminescence, Level Crossing, Rare Earth Ions, Photoionization

Site Specific Relaxation Dynamics of Luminescent Centers

by

Deegala Dorage Mayuri Perera

B.A., University of Peradeniya, 2010

A Dissertation Submitted to the Graduate Faculty
of The University of Georgia in Partial Fulfillment
of the
Requirements for the Degree

Doctor of Philosophy

Athens, Georgia

2016

Site Specific Relaxation Dynamics of Luminescent Centers

by

Deegala Dorage Mayuri Perera

Approved:

Major Professor: Uwe Happek

Committee: Tho Nguyen
Zhengwei Pan

Electronic Version Approved:

Suzanne Barbour
Dean of the Graduate School
The University of Georgia
August 2016

Acknowledgments

I would like to thank my family in Sri Lanka and also my loving husband Daniel and his mother for being a part of my life and uplifting my sprits throughout my graduate life. I would like to thank my advisor, Dr. Uwe Happek, for providing me ample freedom to study, explore different fields other than Physics and broaden my knowledge and also supervising me to have a greater understanding of experimental condensed matter physics. I would also like to thank General Electric (GE) for providing numerous samples for testing. Thank you to all of my colleagues at Physics and Astronomy UGA, for supporting me with various discussions and suggestions.

Contents

List of Figures

List of Tables

Chapter 1

Introduction

Solid state lighting (SSL) as opposed to incandescent or even fluorescent lighting is known to be much more efficient and comes with many advantages for its users. Low power consumption, low maintenance cost, and longer life time are few of the advantages achieved with solid state lighting. Due to these benefits, light-emitting diodes (LEDs) play an important role in the lighting industry.

The success of solid state lighting is the result of rapid development of novel phosphor materials which were necessary because phosphors for fluorescent lighting are optimized for UV excitation, while SSL phosphors are excited in the blue spectral region. Moreover, unlike fluorescent lamps where waste heat is dissipated over the large surface of the lamp tube, waste energy in LEDs are emitted over a very small area which can lead to substantial temperatures in the phosphor coating and to thermal quenching which reduces the performance of LEDs. Advances in the development of efficient phosphors are ongoing, driven by a quest for even higher efficiency and better emission qualities, or by simply finding an equivalent phosphor to one that is protected by patents. In order to aid the development of LED phosphors, fundamental studies can reveal the limitations of these materials by providing a basic understanding of the underlying physical and chemical processes.

While efficiency of an LED is largely controlled by the semiconductor chip, the color quality of the LED is almost entirely dependent on the phosphor that is used. The basic approach in white light LED is to coat a blue LED with a phosphor layer that absorbs part of the blue LED light and converts it to light in the green to red spectrum. The spectrum emitted by the coated LED will then contain a blue component from the LED light that is not absorbed by the coating and the green to red emission of the coating, resulting in a perception of white light.

In order to achieve good color rendering, i.e. an object illuminated by a solid state lighting device looks the same as it appears in sun light, the emission spectrum needs to cover the entire visible range. This can be achieved either by having a phosphor blend or by broadening the emission spectrum of an impurity by introducing disorder into the host material. By carefully tuning a mixture of different phosphors, the color quality of the LEDs are improved, and the "shade" of white can be influenced from blue (cold) white to red (warm) white by changing the ratio of say, green to red emitting phosphors in the blend. This approach will achieve the combination of color rendering and efficiency. A draw-back can be a difference in the degradation of the various phosphors in the blend, resulting in a change of color over time.

A simpler approach is to use a single impurity ion, as it is done in cerium doped $Y_3Al_5O_{12}$. Here the disadvantage lies in the low emission in the red spectral region. This can be overcome by introducing disorder into the host material. Disorder in the host material results in luminescent ions in a number of different local environments and thus crystal fields and symmetry, leading to a marked difference of the emission spectrum from inequivalent sites and to a broadening of the spectrum. The consequences of this approach is analyzed in detail in this dissertation.

An efficient approach to analyzing the effect of the host on the energy levels of an impurity ion is the so-called ligand field theory. This model takes into account the actual orbitals of

the various electron states while treating the neighboring ions (ligands) as point charges. This approach leads to acceptable results as long as covalent bonding can be neglected (thus this approach is not suited for organic compounds).

Cerium, which is a rare earth ion, is most commonly incorporated into materials in its trivalent state. Rare earth ions are ions that are characterized by a Xenon-like electron structure with a partially filled 4f shell. Optical line spectra of these ions arise from transitions between levels of the $4f^n$ configuration [28]. In general, the processes active for the relaxation of rare earth ions in excited electronic states include radiative decay, nonradiative decay wherein the excitation energy is converted into vibrational quanta of the surrounding, nonradiative transfer of energy between like and unlike ions with possible degradation of the excitation and photoionization. These relaxation phenomena for Ce^{3+} ion in $Y_3Al_5O_{12}$ (YAG) and $Na_2Gd_2O(BO_3)_2$ (NABO) are of interest. Our objective is to better understand the luminescence quenching mechanisms of YAG:Ce and NABO:Ce. We focus on luminescence quenching due to level crossing and photoionization. A well-established method to determine the luminescence quenching is to measure the luminescence lifetime as a function of temperature. Therefore, pulsed luminescence experiments were carried out on each of the host materials. A major portion of our work is on YAG:Ce due to its stability and high demand in industry.

In the search of UV transparent materials and/or lasing properties, borates, ***oxyborates***, or fluoride borates represent attractive candidates [1,3–7]. Here, we study sodium gadolinium oxyborate doped with Ce (NABO:Ce). NABO possess two distinct sites of Gd^{3+} where the crystalline environment is different and thus will provide different luminescence quenching probabilities of the dopant ion. Although NABO:Ce does not have much promising benefits due to its low quenching temperatures, studies on NABO were carried out with an intention of understanding its luminescence quenching mechanism.

In this dissertation, the relaxation dynamics of different fluorescent centers and their quenching mechanisms for two different materials (YAG:Ce and NABO:Ce) are discussed in detail. Chapter two focuses on the theoretical background related to our work such as discussions on spectroscopic properties of rare earth doped materials and quenching mechanisms like photoionization and level crossing. Chapter three is focused on work done on yttrium aluminum garnet doped with Ce (YAG:Ce^{3+}). Here, we focus on luminescence quenching of low and high concentrations of YAG:Ce. Detailed description on the experimental set up, our findings and conclusions are included in this chapter. Similar to chapter three, chapter four focusses on the work done on sodium gadolinium oxyborate doped with Ce (NABO:Ce^{3+}). Here, the differences between YAG and NABO and how the luminescence properties change according to the environment and different sites that Ce^{3+} can occupy are discussed in detail.

References

[1] L. Riseberg and M. J. Weber (1975) Progress in Optics **14** (ed. E. Wolf) North Holland, Amsterdam.

[2] C. Corbel, M. Leblanc, E. Anti-Fidancev and M. Lemaitre-Blaise, J. Solid. St. Chem., 144 (1999) 35.

[3] C. Chen, B. Wu, A. Jiang, and G. You, Scientia Sinica, B 28, 235 (1985).

[4] C. Chen,Y. Wu,A. Jiang,B. Wu,G. You,R. Li,and S. Lin,J.Opt.Soc. Am. B 6, 616 (1989).

[5] T. Y. Fan and R. L. Byer, IEEE J. Quant. Electr. 24, 895 (1988).

[6] L. P. Soloveva and V. V. Bakakin, Kristallografija 15, 922 (1970).

[7] R. Norrestam, M. Nygren, and J.-O. Bovin, Chem. Mater. 4, 737 (1992).

Chapter 2

Theoretical Background

A majority of interesting optical properties and applications of solid state materials depend on the presence of optical centers. These centers comprise of dopant atoms that are consciously introduced into the crystal during the growth process, or lattice defects that are created by numerous methods. In this chapter, some general principles specific to optical centers in crystalline host materials are discussed.

Electron-phonon interaction between the electronic states of the dopant atoms and the vibrational modes of the host lattice often gives rise to broad vibronic bands. This is the case when the exited state response to the vibrating environment differs from that of the ground state. Figure 2.1 shows the optical transitions between the ground state of an isolated atom against the optical transitions when it is inserted into a crystalline host material. The presence of electron-phonon coupling associates a continuous band of phonon modes with each electronic state as shown in Figure 2.1(b). In a vibronic system the emission generally occurs at a lower energy level than absorption. This phenomenon is known as the stokes shift. According to Figure 2.1(b), it is clear that the stokes shift arises from the vibrational relaxation that takes place within the vibronic bands.

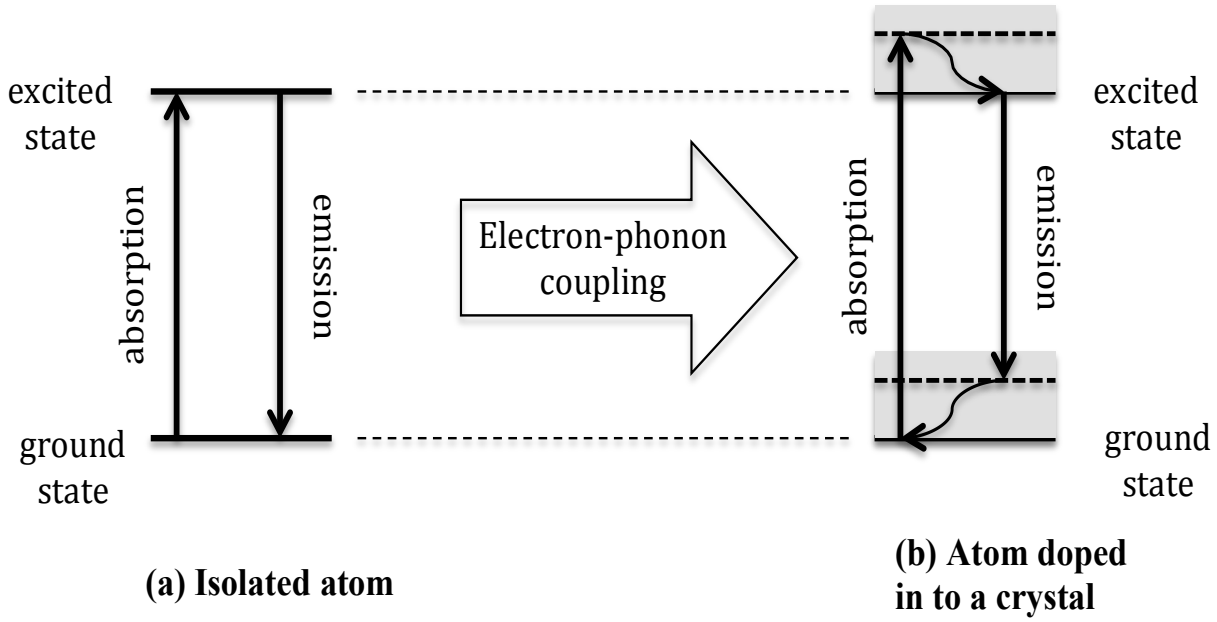

Figure 2.1: (a) Optical transitions between the ground state and excited state of an isolated atom. (b) Absorption and emission in a vibronic solid, in which the electron-phonon interaction couples each electronic state to a continuous band of phonons [1].

Figure 2.2 is a configuration diagram showing the optical transitions in a vibronic solid. Here, the optical transitions are shown by vertical arrows on the diagram (Franck-Condon principle) and it is assumed that the electronic states are bound. At low temperatures, the absorption begins at the lowest vibrational level of the ground state, while the emission originates at the lowest vibrational level of the excited state. The transitions from the lowest vibrational level of the ground state to the lowest level of the excited state are known as zero-phonon lines. Further, mirror symmetry is observed between the emission and absorption about the zero-phonon line [1].

In the static crystal field approach, each ion is assumed fixed at a mean lattice position. The way in which the static crystal field is set up is highly depended on the nature of the crystal. There are many spectroscopically interesting electronic centers in inorganic solids, including single- and multi-vacancy centers in ionic crystals, recombination centers in semiconductors, molecular ions and multi-electron impurities such as transition metal and rare-earth ions. However, there is no common approach to the calculation of the energy levels of these centers [10]. In practice, significantly different methodologies are used for different centers.

2.1 Nonradiative Transitions

The following topics will rely heavily on the text by J. Garcia Sole, L.E. Bausa and D. Jaque [1] and Riseberg and Weber (1975) [28].

When an optically excited center reaches its ground state by other means than emission of photons, it is known as a nonradiative transition. Following is a brief discussion on such nonradiative processes.

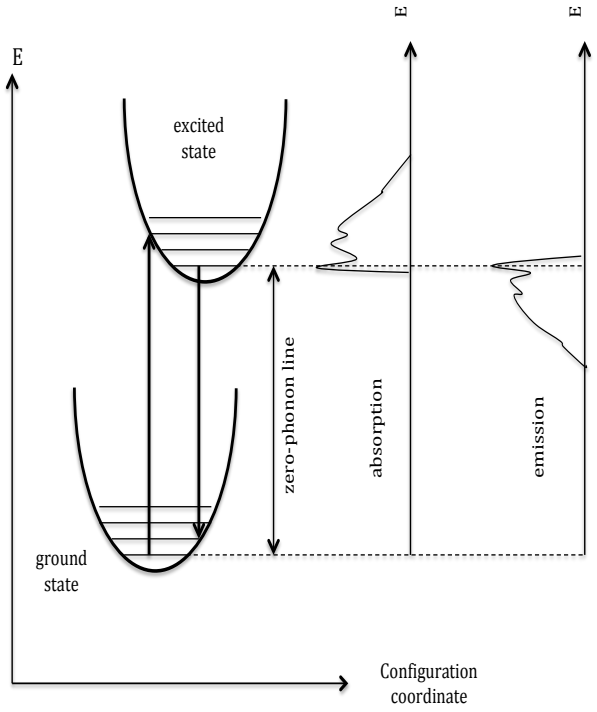

Figure 2.2: Configuration diagram for the ground state and one of the excited electronic states of a vibronic solid. The right hand side figure shows the general shape of the absorption and emission spectra that would be expected [1].

Multiphonon Emission

In Figure 2.3 two configurational coordinate diagrams, corresponding to the case of strong electron-lattice coupling have been displayed. In both cases, the crossover point, X, between the parabolas of the initial (i) and final (f) states are indicated. This point is degenerate in energy, as it belongs to both the ground and the excited state parabolas.

In Figure 2.3 (a), the line AB corresponds to the maximum of the absorption spectrum at 0 K. Here, note that point B is below the crossover point X. The AB absorption process is followed by a fast-down relaxation by multiphonon emission to the point C, from which the emission originates. Thus the emission spectrum has its maximum at an energy corresponding to the line CD. Finally, another multiphonon emission process takes place by down-relaxation from D to A.

In Figure 2.3 (b), which corresponds to a higher Huang-Rhys parameter, the crossover point X is at lower energy than point B. Thus, the center is down-relaxed by multiphonon emission to the vibrational state corresponding to the crossover point X. From this vibrational level the de-excitation probability is much larger through the phonon states of the parabola i than through the phonon states of parabola f. Therefore, as the vibrational level corresponding to point C is not populated, luminescence does not take place. The system returns to the ground state by means of a full nonradiative multiphonon relaxation.

The following section provide another approach to explain multiphonon relaxation. Here, a simple single-phonon frequency model is discussed. However, it is understood that it assumes only one phonon frequency ("effective" phonon frequency) from the continuous spectrum for the non-radiative transition. Nevertheless, this method has proven successful in studies of non-radiative decay of rare-earth ions (Moos 1970 [29] and Weber 1973 [28]).

Figure 2.4 shows radiative and non-radiative decay processes from an excited state to the ground state with transition rates Γ_r and Γ_{nr} respectively. The rate of multiphonon relaxation is temperature dependent due to stimulated emission of phonons as the phonon

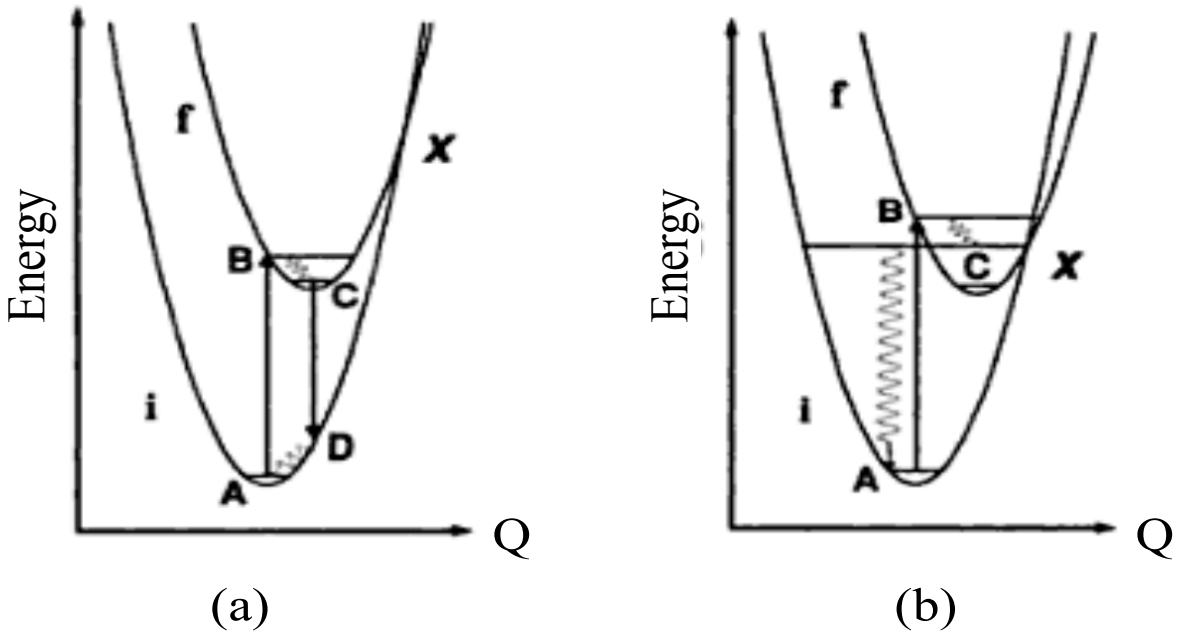

Figure 2.3: Configurational coordinate diagrams to explain (a) radiative and (b) nonradiative (multiphonon emission) de-excitation process. The sinusoidal arrows indicate the non radiative pathways. Image obtained from J. Garcia Sole, L.E. Bausa and D. Jaque [1]

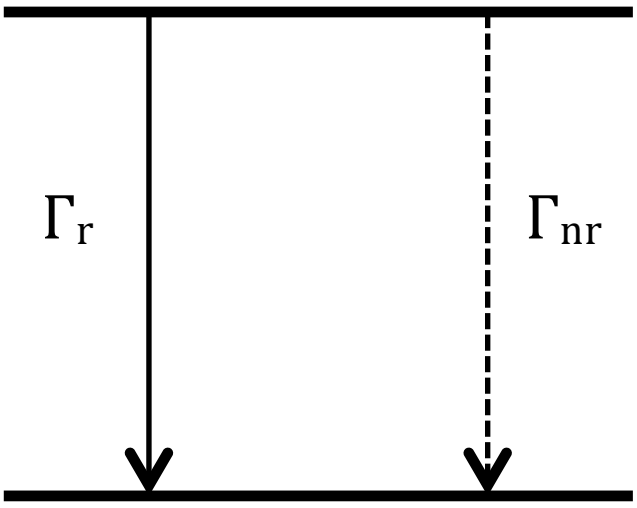

Figure 2.4: Radiative and non-radiative decay processes [10].

modes become thermally populated. A simple single-frequency phonon model frequently yields good agreement with experimental observation [28]. Consider a multiphonon relaxation across an energy gap ΔE to the next lowest level. The number of phonons p_i of equal energy $\hbar\omega_i$, required to conserve energy, and hence the order of the process, is determined by the condition $p_i\hbar\omega_i = \Delta E$. The temperature dependence of nonradiative decay rate is given by the following equation.

$$\Gamma_{nr}(T) = \Gamma_{nr}(0)(n_i + 1)^{p_i} \tag{2.1}$$

Where n_i is the occupation number of the i^{th} phonon mode and $\Gamma_{nr}(0)$ is the spontaneous transition rate, that is, $\Gamma_{nr}(T) = \Gamma_{nr}(0)$ at T=0 K. Replacing n_i by Bose-Einstein average;

$$n_i = \frac{1}{e^{\frac{\hbar\omega_i}{kT}} - 1} \tag{2.2}$$

Then the temperature dependent multiphonon transition rate for a single-frequency p_i-phonon process becomes;

$$\Gamma_{nr}^{p_i}(T) = \Gamma_{nr}(0)\left[\frac{e^{\frac{\hbar\omega_i}{kT}}}{e^{\frac{\hbar\omega_i}{kT}} - 1}\right]^{p_i} \tag{2.3}$$

Thus we obtain;

$$\Gamma_{nr}^{p_i}(T) = \Gamma_{nr}(0)\left[\frac{1}{1 - e^{-\frac{\hbar\omega_i}{kT}}}\right]^{p_i} \tag{2.4}$$

$$\Gamma_{nr}^{p_i}(T) = \Gamma_{nr}(0)\left(1 - e^{-\frac{\hbar\omega_i}{kT}}\right)^{-p_i} \tag{2.5}$$

It is evident from the above equations that the critical feature in the temperature dependence of the multiphonon transition rate is the order of the process p_i.

Energy Transfer

This section on energy transfer is based on "Optical Spectroscopy of Inorganic Solids" by Henderson and Imbush. To analyze the phenomenon of energy transfer as it is experimentally observed one must look at two distinct aspects, one microscopic and the other macroscopic. It is important to understand the microscopic process in which energy of one ion is transferred to a nearby ion, and then estimate the macroscopic behaviour of a very large number of randomly distributed ions in the material since that is what is observed experimentally.

The microscopic energy transfer process in inorganic materials was first considered theoretically by Forster (1948) and Dexter (1953). The excitation is transferred from a donor ion, D, to an acceptor ion, A, separated by a distance R. Schematic energy levels and transitions are shown in Figure 2.5 in which an asterisk indicate an excited state. It is assumed that the radiative emission transition D*→ D and the radiation absorption transition A → A* have the normalized line shape functions $g_D(E)$ and $g_A(E)$ appropriate to homogeneously broadened transitions. Initially the two ions are in the state $|D*, A>$. An interaction $\mathcal{H}'$ between the ions causes a transition from $|D*, A>$ to $|D, A*>$.

The transition probability is given by;

$$W_{DA} = \frac{2\pi}{\hbar}| < D, A^*|\mathcal{H}'|D^*, A > |^2 \int g_D(E)g_A(E)dE \tag{2.6}$$

Here, the overlap integral reflects the requirement of energy conservation.

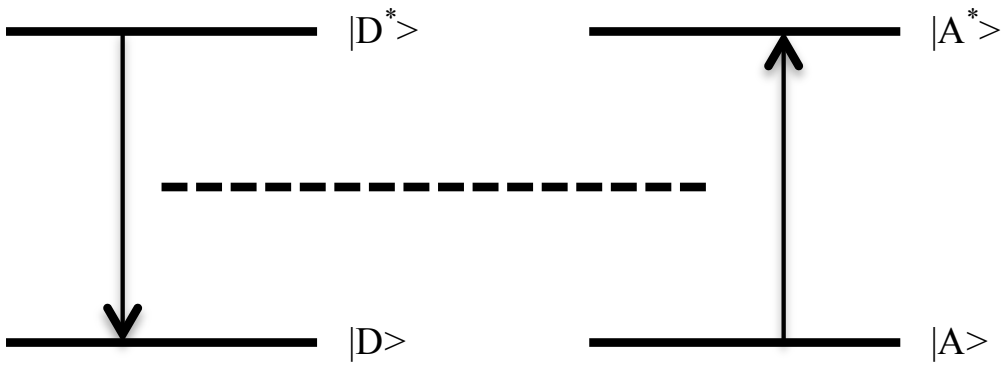

Figure 2.5: Energy maybe transferred from donor ion D, to a acceptor ion, A, by a non radiative process which is analogous to a simultaneous emission process on D and an absorption process on A.

This process is non-radiative; it does *not* involve the emission of light by D and the subsequent absorption by A. Rather it is a simultaneous deactivation of D and activation of A.

2.2 Concentration Quenching of Luminescence

In principal, an increase in the concentration of luminescent centers in a given material should be accompanied by an increase in the emitted light intensity (due to the corresponding increase in absorption efficiency). However, such behavior occurs up to a certain critical concentration of the luminescent centers. Above this concentration, the luminescent intensity starts to decrease. This process is known as concentration quenching of luminescence. Two mechanisms are generally invoked to explain the luminescence concentration quenching.

(i) Quenching Traps - defects or trace ions in the material that can act as acceptors so that the excitation energy can be transferred to them. They act as energy sinks within the transfer chain and so the luminescence become quenched.

(ii) Cross Relaxation - occurs by resonant energy transfer between two identical adjacent centers. In this situation, one of the centers would act as a donor and the other act as an acceptor. Cross relaxation is possible only if there exist a particular energy-level structure between the luminescent centers.

The easiest way to detect luminescent concentration quenching is to analyze the lifetime of the excited centers as a function of the concentration. The critical concentration is that for which the lifetime starts to be reduced.

2.3 Thermal Quenching of Luminescence

In this dissertation the decrease of the luminescence lifetime when the temperature is increased is adressed as thermal quenching of luminescence. This shortening can be due to the change in the probability of radiative transitions or to the increase of the probability of non-radiative transitions.

In the case where there exist a multi-ponon relaxation process, one way to analyze the luminescence lifetime is to use the single phonon frequency model which was discussed in section 2.1.

If the total luminescence lifetime is given by $\frac{1}{\tau_T} = \Gamma_r + \Gamma_{nr}$ where Γ_r and Γ_{nr} are radiative and non-raidative transition rates respectively. Using equation 2.5 total lifetime becomes;

$$\frac{1}{\tau_T} = \frac{1}{\tau_r} + \Gamma_{nr}(0)\left(1 - e^{-\frac{\hbar\omega_i}{kT}}\right)^{-p_i} \tag{2.7}$$

$$\tau_T = \left[\frac{1}{\frac{1}{\tau_r} + \Gamma_{nr}(0)\left(1 - e^{-\frac{\hbar\omega_i}{kT}}\right)^{-p_i}}\right] \tag{2.8}$$

2.4 Absorption and Excitation

The following section is based mostly on the books by Henderson and Imbusch, Vij, Gaft, Reisfeld and Panczer [5–7, 10].

Absorption

Absorption is a measure of the interaction of electromagnetic radiation with matter. Absorption spectroscopy provides information on the wavelengths of electromagnetic radiation that can be absorbed by samples under study. This is determined by varying wavelength and recording the intensity of the transmitted beam.

Light absorbed (at any wavelength) per unit length in a sample is proportional to the light intensity as shown below (Beer and Lambert).

$$\frac{dI(\lambda)}{dx} \propto -I(\lambda) \tag{2.9}$$

$$\frac{dI(\lambda)}{dx} = -\alpha(\lambda)I(\lambda) \tag{2.10}$$

where $\alpha(\lambda)$ is a proportionality constant called the absorption coefficient.
Integrating above equation, the attenuation of a light beam traveling in a medium is given by:

$$I_T(\lambda) = I_0(\lambda)e^{-\alpha(\lambda)d} \tag{2.11}$$

where $I_T(\lambda)$ is the transmitted light intensity, $I_0(\lambda)$ is the incident light intensity, $\alpha(\lambda)$ is the absorption coefficient and d is the length of the light path in the sample.

Thus, the transmittance spectrum and the absorption coefficient are given by following equations.

$$T(\lambda) = \frac{I_T(\lambda)}{I_0(\lambda)} \tag{2.12}$$

$$\alpha(\lambda) = \frac{1}{d} ln \frac{I_0(\lambda)}{I_T(\lambda)} \tag{2.13}$$

Excitation

In an excitation spectrum, the wavelength of the exciting light is varied and the intensity of the emitted light at a fixed emission wavelength is measured as a function of the excitation wavelength. The excitation spectrum gives information on the position of the excited states and crystal field splitting.

The sample luminescence, $S(\lambda)$, as it relates to the Beer-Lambert law is:

$$S(\lambda) = CI_0(\lambda)(1 - e^{-\alpha(\lambda)d}) \tag{2.14}$$

where C is a constant depending on the experimental details. If $\alpha(\lambda)d$ is much smaller than 1, we can Taylor expand the second term of the right site of the equation. This enables us to relate the absorption coefficient to the emission intensity.

$$S(\lambda) = CI_0(\lambda)\alpha(\lambda)d \tag{2.15}$$

2.5 Photoionization and Charge Transfer

This section is based on Bo Wen, "Thermally Stimulated Luminescence Excitation Spectroscopy as a Technique to Measure the Photoionization Energy of $Sr(SCN)_2$:Eu^{2+}."

Electron transfer processes are defined here as charge transport between an impurity ion and the host valence or conduction bands and the band-to-band excitation that generates electron hole pairs. Traditionally, the transfer of an electron from the valence band to the impurity is called a charge transfer process. The promotion of an impurity electron into the host conduction band is called photoionization. The latter process is sometimes called metal-to-metal charger transfer process. These three processes are shown in Fig. 2.6. Transition (a) corresponds to a band-to-band excitation, that occurs for photon energies $h\nu \geq E_{gap}$. Transition (b) corresponds to the photo-ionization of an impurity ion, producing an electron in the conduction band and an oxidized ion. Transition (c) corresponds to a charge transfer process: the promotion of an electron from the valence band to an impurity ion, producing a free hole in the valence band and a reduced ion.

Electrons and holes generated in these processes can migrate within the lattice until they recombine (Fig. 2.7, d,e, and f). Another possibility is the capture of the carriers by electron or hole traps. Traps can be classified as deep or shallow traps, where deep and shallow are not absolute characteristics, but describe the depth of a trap relative to kT at a given temperature. So far all the discussion about electron transfer processes are concerned with transitions involving the delocalized bands. For example, in Figure 2.7, transition (f) involves relaxation of an electron from the conduction band to the impurity ion. In most relevant cases, however, the relaxation process will include the occupation of an excited impurity level, followed by impurity specific luminescence to the ground state (transition (j), Fig. 2.8). The rare earths are good examples of substances which exhibit transition (j).

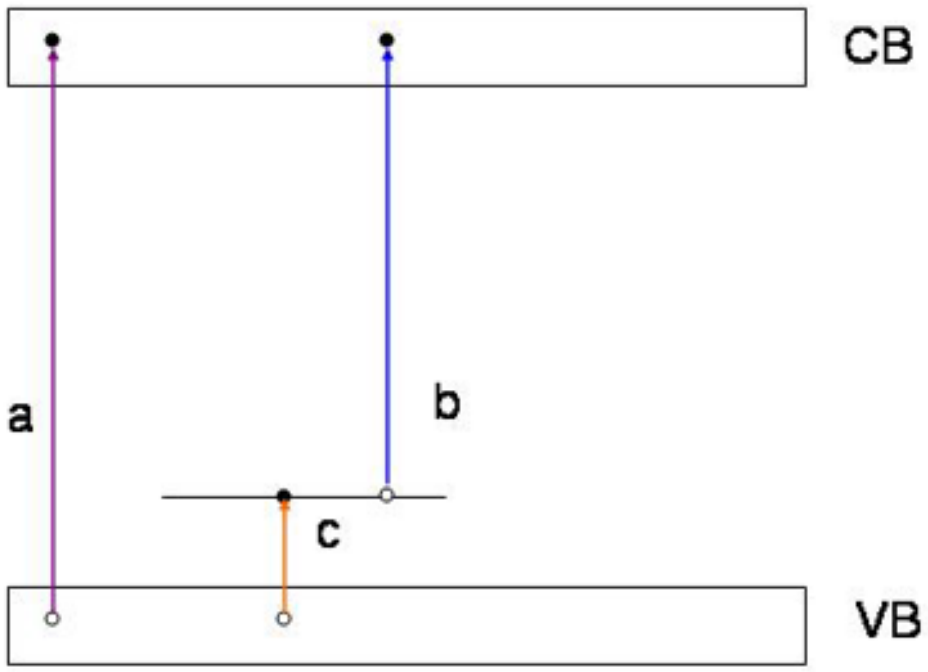

Figure 2.6: Electron transitions in insulators:(a) band to band excitation; (b)photoionization; (c)charge transfer; Electrons, solid circles; holes, open circles [23].

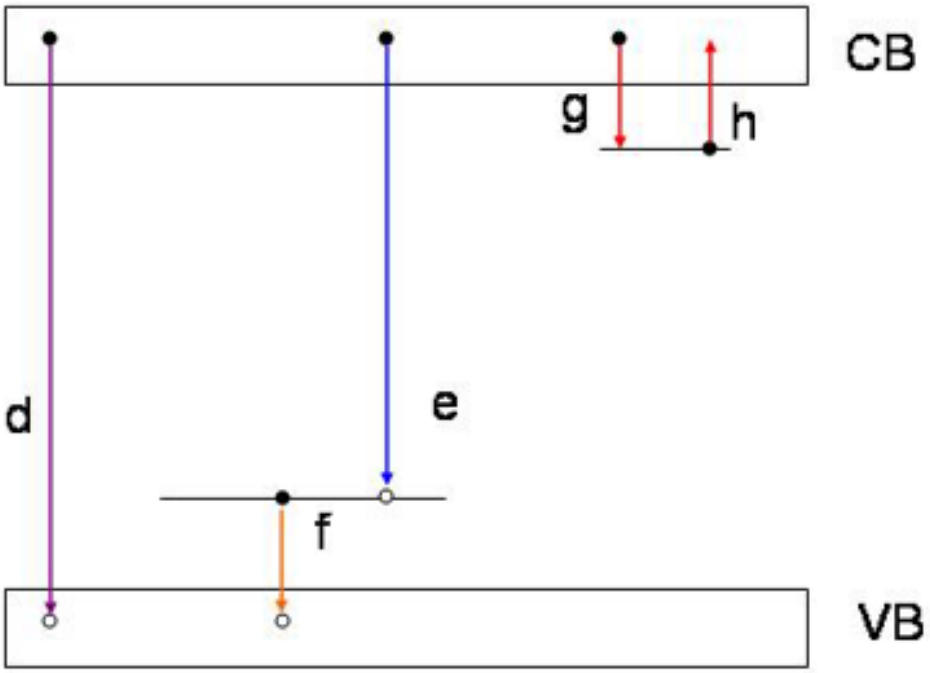

Figure 2.7: Electron transitions in insulators:(d) (e) and (f) are radiative or nonra- diative relaxation. (g) trapping (h) untrapping ;Electrons, solid circles; holes, open circles [23].

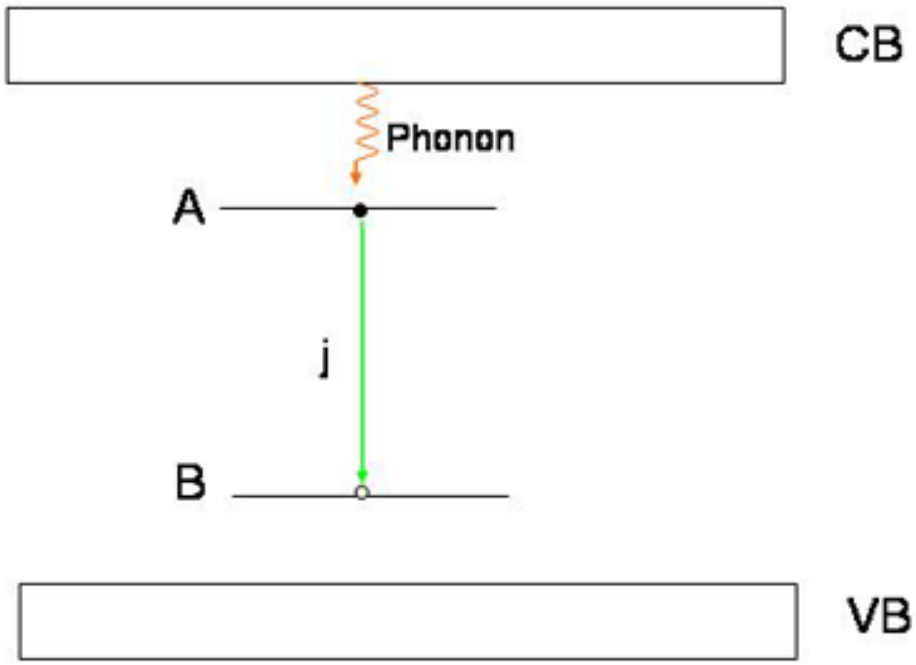

Figure 2.8: Electron transitions not involving the conduction or valence bands. Electrons-solid circles; Holes-open circles [23].

2.6 The Rare Earths and Garnets

Rare-earth elements (REs) are also called Lanthanides. These are used in many light-based applications based on their luminescence (lasers, LEDs, displays etc.). Rare earth elements have an electronic configuration $4f^n\ 5s^2 5p^6\ 6s^2$. The optically active 4f electrons of the rare earth ions are shielded by the outer, though less energetic, 5s and 5p shells of electrons. As a result the optically active 4f electrons of rare-earth ions in solids are not strongly affected by neighbouring ligands. If the neighbouring ligands are neglected the energy levels of the 4f electrons are just the free ion levels. The energy levels of free ions are very sharp [10]. Despite of relatively similar properties of the REs, the lattices formed by RE ions do not all exhibit similar behavior [16, 21]. These differences arise from the increasing number of $4f$- electrons as one moves from La to Lu and the fact that these electrons are capable of forming localized electronic states in the forbidden band-gap.

In the past, the rare earths were actually rare and difficult to obtain pure. In the present however, modern methods have made it possible to obtain all rare earths highly pure and in substantial quantities at quite reasonable prices [6]. The optical properties of trivalent rare earths are much more important than neutral atoms. In the triply charged rare-earth ions all 5d and 6s electrons are removed and the 4f shell is only partially occupied; Table 2.1 gives the number (n) of the electrons in the unfilled 4f shell. Figure 2.9 shows the energy levels of trivalent rare-earth ions in lanthanum trichloride ($LaCl_3$) which were determined by Dike and his co-workers.

Lanthanum possess closed shell configurations in its trivalent state (corresponding to [Xe]) and therefore do not have any occupied levels above the core levels. La^{3+} forms a localized (unpopulated) $4f$-state between the Fermi level at mid gap and the bottom of the CB [17, 18]. Ce^{3+}, Pr^{3+} and Nd^{3+} are all known to have the localized (populated) f-levels between Fermi energy and the top of the VB in oxides, fluorides and sulfides [19, 20]. These

Table 2.1: Number of electrons (n) in the 4f shell of triply charged rare-earth ions [10].

	n
Ce^{3+}	1
Pr^{3+}	2
Nd^{3+}	3
Pm^{3+}	4
Sm^{3+}	5
Eu^{3+}	6
Gd^{3+}	7
Tb^{3+}	8
Dy^{3+}	9
Ho^{3+}	10
Er^{3+}	11
Tm^{3+}	12
Yb^{3+}	13

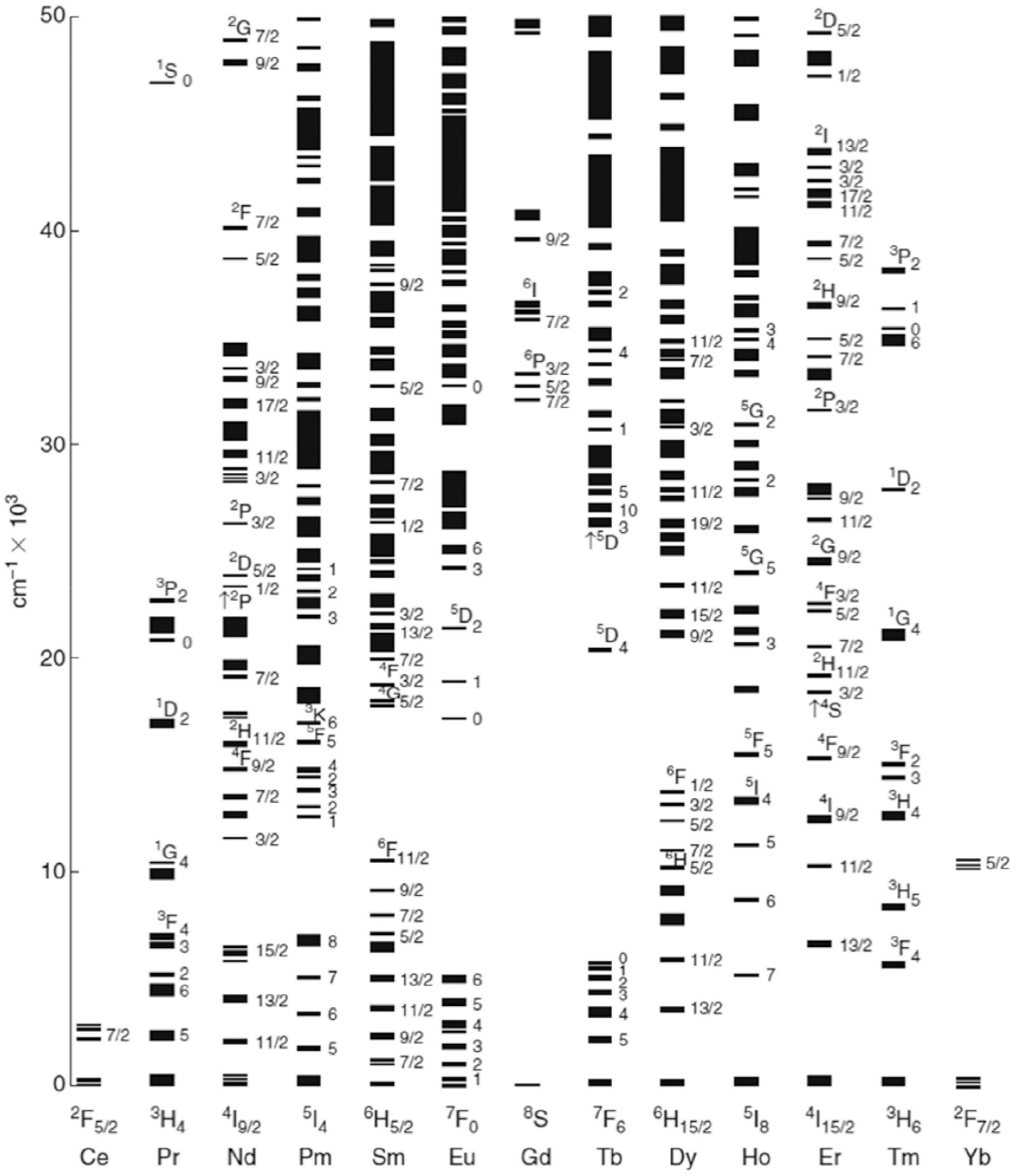

Figure 2.9: Dieke diagram for rare earth ions. The thickness of each level represents the total crystal splitting in $LaCl_3$. A pendant semicircle indicates that this level fluoresces in the $LaCl_3$ structure.

levels cause smaller cut-off energies in the visible spectrum compared to the rest of the RE compounds. Most garnets can be described in terms of a body centered cubic unit cell of the $Ia\bar{3}d$ (230) space group, which contains eight formula units of $A_3B'_2B''_3O_{12}$. A, B′ and B″ are cations of different nominal charges in different symmetry sites [3].

2.7 Luminescence in rare-earth compounds

Luminescence is the emission of light from a system that is excited by some form of energy. In some ways, luminescence can be considered as the inverse process of absorption [1]. Luminescence can occur by a number of mechanisms [1]. Depending on the different mechanisms, the types of luminescence varies. Photoluminescence, cathodoluminescence, electroluminescence, chemiluminescence, bioluminescence etc. Photoluminescence occurs after excitation with light. Excitation with an electron beam is called cathodoluminescence and so on.

In the case of photoluminescence, the ratio between the emitted and absorbed photons represent the luminescent efficiency or quantum efficiency (η) [1]. The following equation gives a relationship between the emitted (I_{em}), incident (I_0) and absorbed (I) intensities and the luminescent efficiency η.

$$\eta = \frac{I_{em}}{I_0 - I} \tag{2.16}$$

A luminescent efficiency of $\eta < 1$ indicates that a fraction of the absorbed energy is lost by nonradiative processes (discussed in section 2.1). Usually in a luminescence experiment, only a portion of the total emitted light is measured due to experimental restrictions. This fraction depends on the focusing system and on the geometric characteristics of the detector [1]. Equation 2.17 provides a general equation showing the relationship between the measured intensity (I^*_{em}) and the incident intensity I_0. Here, k_g is a geometric factor that depends on

the experimental setup and OD is the optical density of the sample.

$$I^*_{em} = k_g \times \eta \times I_0(1 - 10^{-OD}) \tag{2.17}$$

For low optical densities, the equation 2.17 becomes:

$$I^*_{em} = k_g \times \eta \times I_0 \times (OD) \tag{2.18}$$

The measured intensity's proportionality to optical density which only holds for low optical densities indicate that the excitation spectra only reproduce the shape of absorption spectra for samples with low concentrations.

There are two types of RE-emission:

1. Ground state $4f^n$ - excited state $4f^n$ (f-f emittors)

2. Ground state $4f^n$ - excited state $4f^{n-1}5d$ (d-f emittors)

Among the above, the second d-f emittors strongly depend on the host environment.

2.8 Cerium (Ce)

Cerite, the earliest known of the numerous minerals in which the element cerium occurs, was first discovered in an iron mine at Bastnäs, Westmannlaud, Sweden, in 1750, by Cronstedt [13]. In 1803 specimens of the mineral were sent to Berzelius, and to Klaproth for analysis. These two chemists, at nearly the same time, but independently, isolated the unrecognized mineral. Berzelius, with whom was associated Hisinger, gave it the name Ceria [14]. The first Cerium to be prepared in pure condition, was that made by Wöhler [15] in 1876, by reducing cerous chloride by means of metallic sodium.

Cerium based lattices

Cerium exhibits three oxidation states, +2, +3 and +4. Here, we focus on the +3 oxidation state. Compared to other trivalent lanthanide ions, the energy-level structure of Ce^{3+} is simple [10]. The ground state electron configuration consists of the [Xe] closed shell configuration plus an optically active electron in *4f* shell. The $4f^1$ ground state is separated about 51,000 cm^{-1} from the excited $5d^1$ configuration [24]. In a crystalline environment, the *5d* may split by as much as 25,000 cm^{-1} into at most five distinct *5d* states [10]. In addition the average energy of the five *5d* levels may shift downwards by 22,000 cm^{-1} [2–4, 24]. This downward shift is defined as the centroid shift of the *5d* configuration.

2.9 Madelung Potential

Crystalline solids are roughly classified into five classes: molecular, ionic, covalent, metallic, and hydrogen bonded [10]. A crystal consists of an atom or an arrangement of atoms repeated periodically throughout space. This can be mathematically defined by a space lattice as shown in Equation 2.19 [11]. Here, n_1, n_2, n_3 are integers and $\mathbf{a_1}, \mathbf{a_2}, \mathbf{a_3}$ are primitive vectors.

$$\mathbf{n} = n_1\mathbf{a_1} + n_2\mathbf{a_2} + n_3\mathbf{a_3} \tag{2.19}$$

The following discussion will be based solely on the ionic crystals. Ionic crystals are a class of crystals in which the lattice-site occupants are charged ions. The idealized model of an ionic crystal supposes that the constituents are positive and negative ions bearing charges which are multiples of the electronic charge, with the charge distributed with spherical symmetry on each ion as in the rare gas atoms. The interactions between ions are assumed to be primarily the electrostatic interactions between spherical charge distributions [22]. The simplest ionic crystals are the alkali halides (combining an element from the 1^{st} column of the

periodic table and an element from the 7^{th} column). Lattice energy of an ionic crystal is the energy involved when a crystal is formed from individual ions, rather than from individual atoms [12]. This may also be defined as the energy spent in separating a solid ionic crystal into its constituents.

Sodium chloride (NaCl) crystallizes in the structure shown in Figure 2.10. The space lattice is fcc with one Na^+ and one Cl^- ion with each lattice point. In the crystal each ion is surrounded by six nearest neighbors of the opposite charge and twelve next nearest neighbors of the same charge as the reference ion. If ϕ_{ij} is the interaction energy between ions i and j, the total energy of any one ion is given by Equation 2.20 [22].

$$\phi = \Sigma'_j \phi_{ij} \tag{2.20}$$

Here, the prime indicates that the summation is to include all ions except j = i and ϕ_{ij} is given by Equation 2.21.

$$\phi_{ij} = \frac{\lambda}{r_{ij}^n} \pm \frac{e^2}{r_{ij}} \tag{2.21}$$

Where the + sign is to be taken for like charges and the − sign for unlike charges. r_{ij}-distance between ion i and j, λ and n are constants to be determined from observed values of the lattice constant and compressibility. The value of ϕ does not depend on whether the reference ion i is a positive or a negative ion, and as the sum can be made to converge rapidly its value will not depend on the particular location of the reference ion in the crystal as long as it is not near the surface. Neglecting surface effects, the total lattice energy U_0 of a crystal composed of 2N ions can be written as Equation 2.22.

$$U_0 = N\phi \tag{2.22}$$

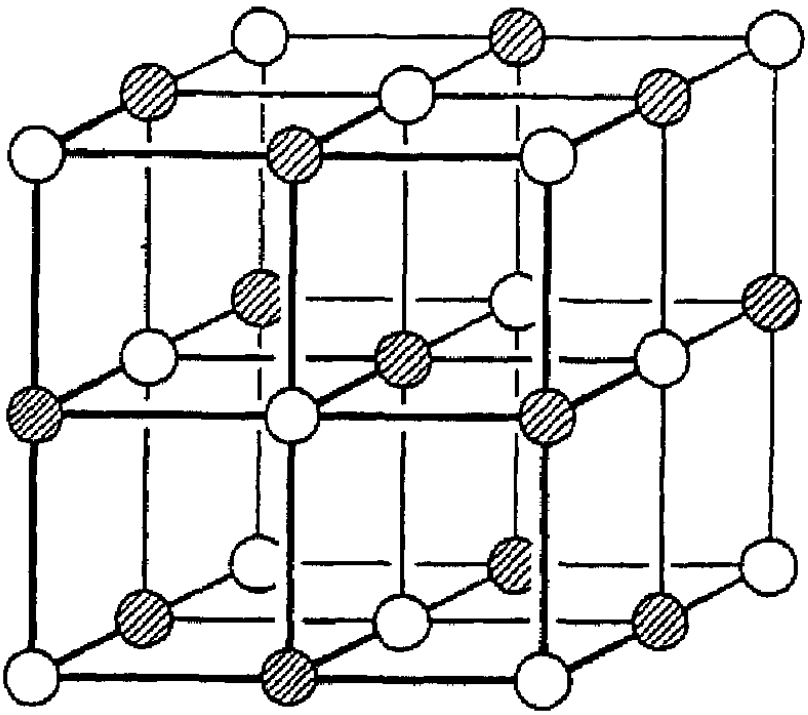

Figure 2.10: Sodium chloride structure

Here, N is used rather than 2N since in taking the total lattice energy interactions per each pair must be counted only once. As mentioned in section 2.5, the total lattice energy U_0 is the energy required to separate the crystal into individual ions at an infinite distance apart. If $r_{ij} = p_{ij}R$, where R is the nearest neighbor distance in the crystal then Equations 2.21 and 2.20 can be written as,

$$\phi_{ij} = \frac{1}{p_{ij}^n}\frac{\lambda}{R^n} \pm \frac{1}{p_{ij}}\frac{e^2}{R} \tag{2.23}$$

$$\phi = \frac{\lambda A_n}{R^n} - \frac{\alpha e^2}{R} \tag{2.24}$$

Where $A_n = \Sigma'_j p_{ij}^{-n}$ and $\alpha = \Sigma'_j \pm p_{ij}^{-1}$. Here, the quantity α is known as the *Madelung Constant* and is a property of the crystal lattice. The Madelung constant is of central importance in the theory of ionic crystals [22]. Further, Figure 2.11 shows the variation of ϕ with R.

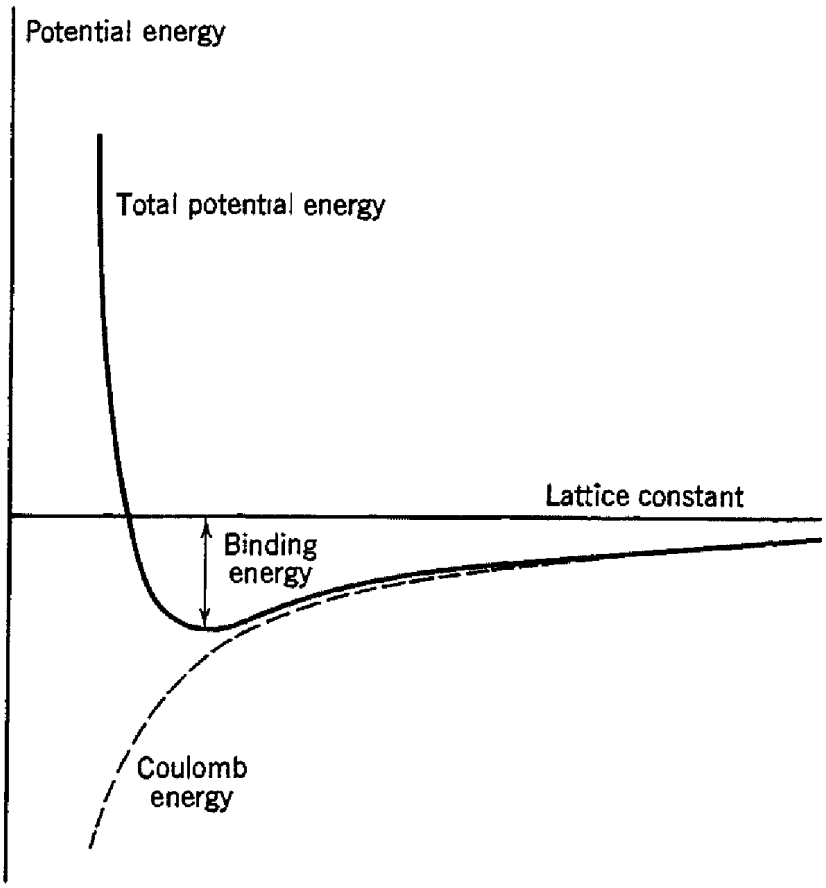

Figure 2.11: Potential energy of an ionic crystal vs. lattice constant [22].

References

[1] Mark Fox,"Optical properties of Solids", *Department of Physics and Astronomy, University of Sheffield.*

[2] J. Garcia Sole, L.E. Bausa and D. Jaque, "An Introduction to the Optical Spectroscopy of Inorganic Solids".

[3] Philippe Smet,"Luminescence and luminescent materials", *LumiLab - Department of solid state sciences - Ghent University.*

[4] B. Henderson and G. F. Imbusch, "Optical spectroscopy of inorganic solids".

[5] D. R. Vij, "Luminescence of Solids", Prenum Press, New York, 1998.

[6] M. Gaft, R. Reisfeld, G. Panczer "Luminescence Spectroscopy of Minerals and Metarials", Springer Press,Berlin, 2005.

[7] Murat Acibin, "Luminescence Properties of Octahedrally Coordinate Eu^{2+} ions", University of Georgia.

[8] Luis Seijo and Zoila Barandiaran, "4f and 5d Levels of Ce^{3+} in D_2 8-fold oxygen coordination" *Optical Materials 35 (2013) 1932-1940.*

[9] G. H. Dieke, "Spectra and Energy Levels of Rare Earth Ions in Crystals".

[10] Michael P. Marder, "Condensed Matter Physics".

[11] J. P. Elliott and P. G. Dawber, "Symmetry in Physics".

[12] A. Kumar, "Introduction to Solid State Physics".

[13] Sv. Vet. Akad. Handl.,1751, s. 227. 4 A. Gehl., 2, 303 ; Beitrage, 4, 140.

[14] Afhandl, I.Fysik, Kemioch Mineral., 1, 58 ; A. Gehl., 2, 397.

[15] Ann. der Chem., 14.4, 251.

[16] V.P. Zhuze, A.I. Shelykh, Sov.Phys.Solid State **23** , 245 (1989).

[17] R.A. Evarestov, A.V. Leko, I.V. Murin, A.V. Petrov, V. A. Veryazov, phys.stat.sol. (b) **170**, 145 (1992).

[18] K.C. Mishra, K.H. Johnson, in *Scintillator and Phosphor Materials, eds.* M.J. Research Society Symposium Proceedings Vol. **384** (Materials Research Society), Pittsburg, 1994) p.367.

[19] M.V. Ryzhkov, V.A. Gubanov, Yu.A. Teterin, A.S. Baev, Z.Phys.B 59, 1 (1985); Z.Phys.B 59, 7 (1985).

[20] C. Pedrini, D. Bouttet, C. Dujardin, A. Belski, A. Vasil'ev, in *Proceedings of the International Conference on Scintillators and Their Applications, SCINT '95,eds.* P. Dorenbos, C.E.W. van Eijk (Delft University Press, Delft, The Netherlands, 1996), p.103.

[21] Madis Raukas; "*Luminescence Efficiency and Electronic Properties of Cerium Doped Insulating Oxides*". University of Georgia.

[22] C. Kittel, "*Introduction to Solid State Physics*".

[23] Bo Wen, "Thermally Stimulated Luminescence Excitation Spectroscopy as a Technique to Measure the Photoionization Energy of $Sr(SCN)_2$:Eu^{2+}" University of Georgia.

[24] P. Dorenbos, "Relating the energy of the [Xe]$5d^1$ configuration of Ce^{3+} in inorganic compounds with anion polarizability and cation electronegativity" DOI: 10.1103/Phys. Rev. B.65.235110.

[25] P.Dorenbos, Phys. Rev. B 62, 15 640 (2000).

[26] P.Dorenbos, Phys. Rev. B 62, 15 650 (2000).

[27] P.Dorenbos, Phys. Rev. B 64, 125117 (2001).

[28] L. Riseberg and M. J. Weber (1975) Progress in Optics **14** (ed. E. Wolf) North Holland, Amsterdam.

[29] Moose, H. W. (1970) J. Luminescence 1,2,106.

Chapter 3

Relaxation dynamics of YAG:Ce^{3+}

3.1 Introduction

The Nobel Prize in Physics 2014 was awarded jointly to Isamu Akasaki, Hiroshi Amano and Shuji Nakamura for the invention of efficient blue light-emitting diodes which has enabled bright and energy-saving white light sources. Yttrium aluminum garnet (YAG) doped with Ce^{3+} is widely used in the market of white light LEDs. Here, we study the luminescence quenching at high temperatures in YAG:Ce for two different Ce concentrations (0.1% and 3%) with the intension of better understanding the quenching mechanism of high concentration, 3% YAG:Ce. These concentrations were chosen because in the 0.1% Ce doped sample, cross-relaxation can be neglected, while in the 3% sample the effect of cross-relaxation is evident.

In the case of high dopant concentrations it is possible that two centers sufficiently close to each other will interact. This interaction maybe significantly strong to enable excitation to be transferred from one to another. This occurrence of energy migration between dopant centers can significantly affect the luminescence properties of a host material.

A shorthand notation of energy transfer rate on transition probability for energy transfer by electric dipole-dipole interaction is given by Equation 3.1 [10].

$$W_{DA}^{dd} = \frac{\alpha_{DA^{(6)}}}{R^6} \tag{3.1}$$

Here, α is a constant term and R is the average distance between two Ce^{3+} ions. According to Equation 3.1, at high concentrations of Ce, when the probability of having another Ce ion nearby gets larger, there exists a large d-d transition probability. Thus in heavily doped YAG:Ce a lower quenching temperature is observed compared to low concentration YAG:Ce. This temperature-dependence of luminescence emission was studied in detail, in order to better understand the quenching mechanism of high concentration YAG:Ce.

This chapter provides a brief theoretical background, a summary on the experimental techniques and materials used in this study. Finally, the experimental results and the conclusions are discussed. Further, we compare our findings with work done by Meijerink *et al.* [11].

3.2 Yttrium aluminum garnet (YAG)

YAG ($Y_3Al_5O_{12}$) can be described in terms of a 160 atom body-centered cubic unit cell with a 80 atom unit cell. In YAG for instance, Yttrium atoms occupy 24 sites of 8-fold coordination [3]. Figure 3.1 and 3.2 shows the unit cell of YAG and the local surrounding of one yttrium atom respectively [4].

Yttrium aluminum garnet $Y_3Al_5O_{12}$ (YAG) doped with Ce^{3+} is a well known phosphor with a blue Ce^{3+} 4f $\rightarrow$ 5d absorption and a corresponding yellow 5d $\rightarrow$ 4f emission [3, 7]. YAG:Ce^{3+} is also a well known scintillating material due to their fast scintillation response

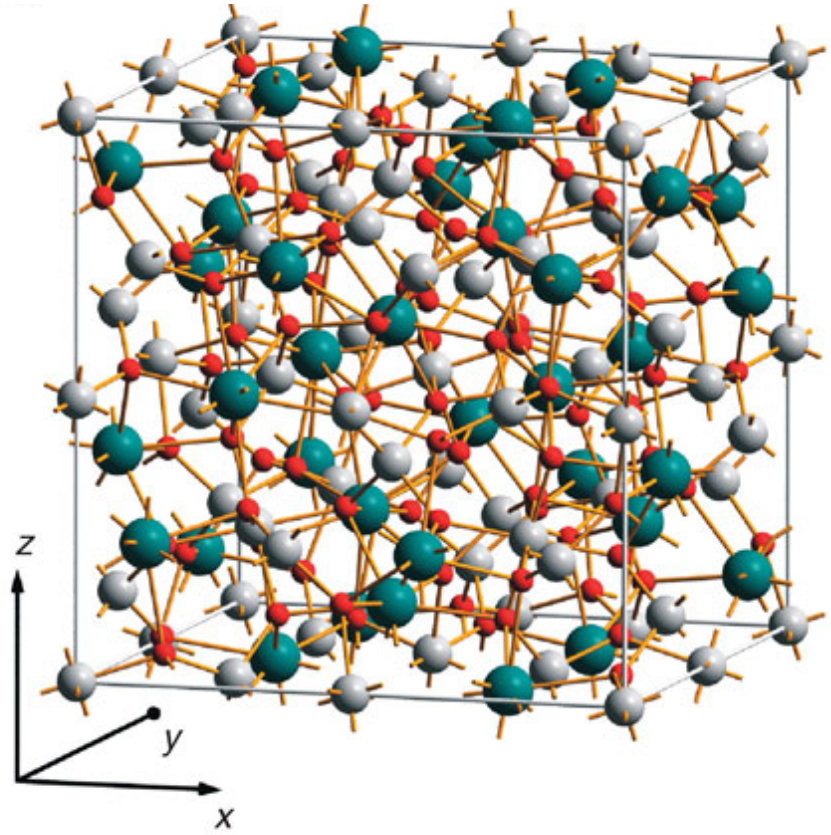

Figure 3.1: Unit cell of YAG crystal. Green, white and red sites are occupied by yttrium, aluminum and oxygen respectively. All together, the unit cell contains eight molecular units of $Y_3Al_5O_{12}$ [3].

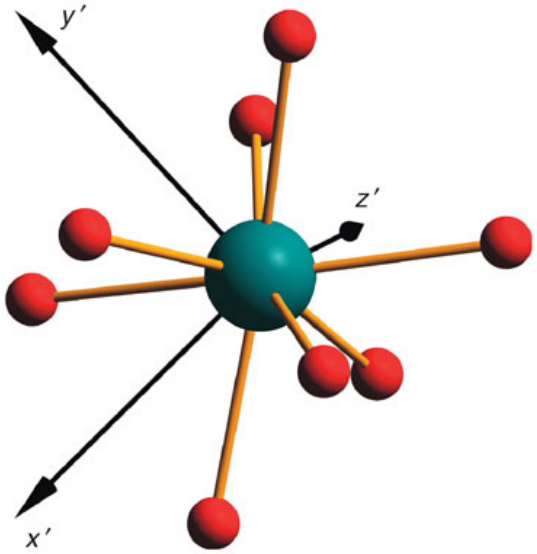

Figure 3.2: The local surrounding of one yttrium site. The local z′ axis is along the y crystal axis, the axes x′ and y′ are rotated with respect to x and z crystal axes by 45° [3].

and high efficiency. In YAG:Ce, the optically active Ce^{3+} dopant ions substitute for yttrium (Y) atoms, which have the local symmetry of D_2 point group and a first coordination shell made of 8 oxygen (O) atoms. The energies of the 4f and 5d levels of Ce^{3+} in particular garnets and in other oxides depend highly on the bonding and electrostatic interactions between Ce and the hosts, and they can be calculated by means of *ab initio* methods [3].

The free ion configuration of Ce^{3+} consists of one ^2F pair of levels ($^2F_{7/2}$ and $^2F_{5/2}$) separated by 2253 cm^{-1} [6]. Under a crystal field, the lower $^2F_{5/2}$ level gets split into a maximum of three components (Z_1, Z_2, Z_3) and the $^2F_{7/2}$ gets split into four (A_1, A_2, A_3 and A_4). Table 3.1 shows the Ce^{3+} energy levels for various host crystals.

Table 3.1: Ce^{3+} energy levels for various host crystals [6].

		$LaCl_3^a$	YGG^b	LaF_3^c	CeF_3^c
$^2F_{5/2}$	Z_1	0.0	0	0.0	0
	Z_2	37.5	139	150.5	82
	Z_3	110.0	402	-	-
$^2F_{7/2}$	A_1	2166.0	2161	2160.5	2158
	A_2	2208.6	2176	2239.5	2238
	A_3	2282.6	2373	2635.3	2638
	A_4	2399.5	3670	2845.0	2848

[a] Hellwege er al. (1965)
[b] Herrmann et al. (1966)
[c] Buchanan et al. (1966)

3.3 Ce doped YAG

Cerium-activated yttrium aluminum garnet (YAG:Ce^{3+}) is one of most popular used phosphors to combine with single blue LEDs to generate white light and also it is one of the phosphors which is heavily studied. The Ce-doped yttrium aluminum garnet, $Y_3Al_5O_{12}$, exhibits intense broad-band green emission from crystal-field split 5d states to the ground 4f state. Here, the ground state yields two multiplets, $^2F_{5/2}$ and $^2F_{7/2}$, due to the spin-orbit

interaction, which are separated by some 0.25 eV in YAG [12]. These multiplets are split in the crystal field of D_2 symmetry of dodecahedral Ce sites. The excited $5d^1$ configuration is split by the crystal field into five components [13]. The emission occurs from the lowest 5d crystal-field component to the $^2F_{5/2,7/2}$ levels of the ground state. A popular method to study the luminescence quenching is to study the temperature dependence of luminescence lifetime.

Studies by Meijerink *et al.* [11] focusses on the luminescence quenching of Ce^{3+} in YAG:Ce. They have studied the temperature dependence of the emission intensity and thus the luminescence lifetimes for a wide range of Ce concentrations in YAG. Their findings suggest that in the case of high concentration of Ce, the reduced quenching temperature compared to low doped samples are caused by rapid energy transfer among cerium ions resulting in excitation loss at an unspecified quenching center.

Based on our work, we suggest that the luminescence quenching mechanism in high concentration Ce is caused by "distorted" cerium sites which have a higher probability of non-radiative relaxation due to level crossing (also known as crossover-mechanism [10, 17]) as compared to the low concentration samples. Here, by the term "*distorted*" we mean to focus on those Ce^{3+} ions of which the surrounding is quite different from that of a low concentration situation. When YAG is doped with Ce, it is known that Ce^{3+} ions occupies Y^{3+} sites [14]. In the case of 3% Ce, there exist a 0.03 probability of having a Ce^{3+} ion at a Y^{3+} site. This probability compared to 0.001 in the case of low concentration situation is high. Thus it is possible to have two or more Ce^{3+} ions sufficiently close to each other in a high doped YAG:Ce crystal than a low doped crystal. In our studies, we specifically target these disturbed sites of Ce^{3+}.

3.4 Pulsed luminescence experiment

Pulsed optical excitation promotes a non-stationary density N of centers into the excited state. These excited centers can decay to the ground state by radiative (r) and non-radiative (nr) processes giving a decay-time intensity signal [1]. Luminescence lifetime (τ) represents the time in which the emitted intensity decays to $1/e$ of the intensity at t=0 (I_0). It is important to note that this lifetime value gives the total lifetime (radiative plus non-radiative). If total decay rate (total decay probability) is denoted by Γ_T, we can write:

$$\Gamma_T = \Gamma_r + \Gamma_{nr} \tag{3.2}$$

Here Γ_r is the radiative rate (which corresponds to radiative lifetime) and Γ_{nr} is the non-radiative decay rate (rate for non-radiative processes) with $\Gamma_r = \frac{1}{\tau_r}$ and $\Gamma_{nr} = \frac{1}{\tau_{nr}}$. If N is the population of the excited state.

$$\frac{dN}{dt} = -(\Gamma_r + \Gamma_{nr})N \tag{3.3}$$

Equation 3.3 gives us $N(t) = N(0)e^{-\Gamma_T t}$, where $N(0)$ is the population of the excited state at t=0.

The de-excitation process can be experimentally observed by analyzing the temporal decay of the emitted light. Since the emitted light intensity is proportional to the population of each states, it also corresponds to an exponential decay law (Equation 3.4) with $\Gamma_T = \frac{1}{\tau_r} + \frac{1}{\tau_{nr}}$.

$$I_{em}(t) = I_0 e^{-\Gamma_T t} \tag{3.4}$$

Where, I_0 is the intensity of light at t=0.

In order to measure the radiative lifetime of a transition it is necessary to use a short excitation pulse in the wavelength region of the appropriate absorption band, together with some means of recording the temporal evolution of the luminescence signal. In our case the emission signal is detected using a photomultiplier. Usually the luminescence yield following a single excitation pulse is too small for good signal-to-noise throughout the decay period. Therefore, repetitive pulsing techniques are used together with signal averaging to obtain good decay statistics. If the pulse is repeated N times then there is an $\sqrt{N}$ improvement in the signal-to-noise ratio.

3.5 Experimental Setup

Life time measurements

Figure 3.3 shows a schematic of the experimental setup used for luminescence decay-time measurements in this study. The YAG:Ce^{3+} sample was placed inside a quartz tube in an optical sample furnace and illuminated with the pulsed radiation of a light emitting diode(LED). The LED was driven at a repetition rate of up to 1 MHz with the output of an Avtech AVP-C pulse generator, boosted by a high frequency Avantech power amplifier. The pulse width of the LED was measured to be 2 ns. A thermocouple is used to measure the temperature of the sample accurately as possible.

Luminescence was detected at right angle with respect to the excitation direction with a Hamamatsu R212 Photo Multiplier(PMT), attached to the optical sample furnace via a light tight tube. An interference filter was inserted in the detection path in order to select a specific detection wavelength. To avoid room light to enter the system, the excitation window of the optical furnace was covered with a narrow band interference filter that selects the appropriate excitation wavelength from the relatively broad LED spectrum.

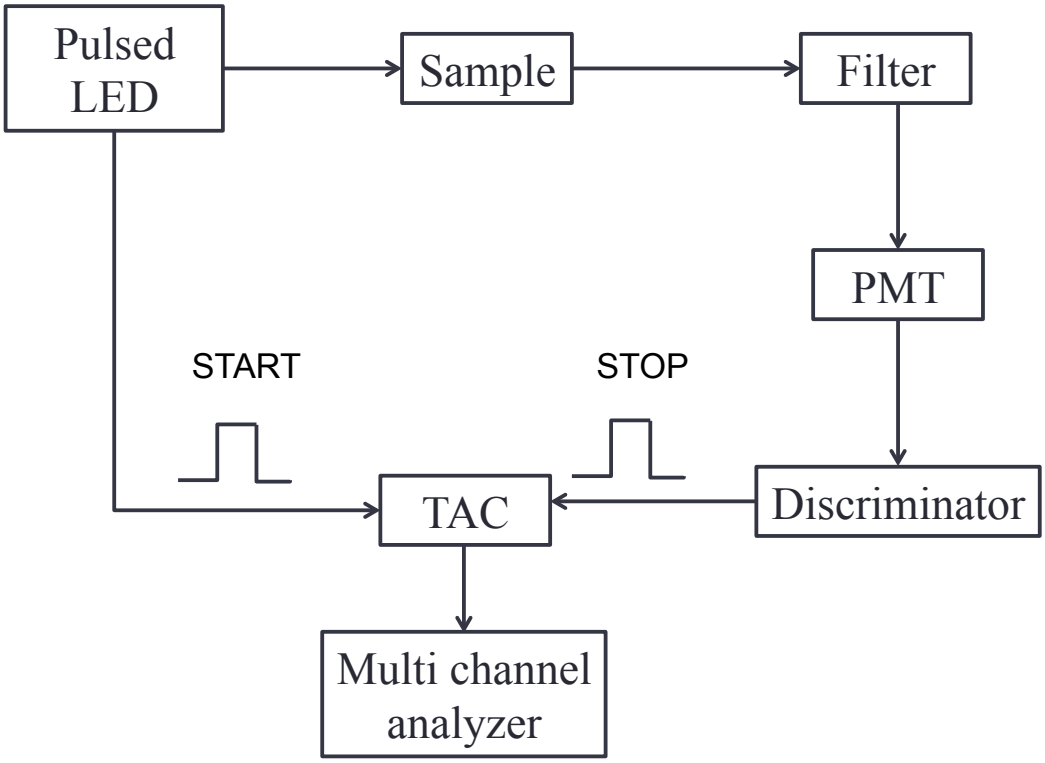

Figure 3.3: Experimental setup. PMT - Photo Multiplier Tube, TAC - Time to Amplitude Converter

The PMT signal was recorded with a photon counting system. The weak photomultiplier pulses are amplified using a 500 MHz high frequency amplifier and the output of the amplifier is fed in to a discriminator which generates square pulses. Weak dark counts and amplifier noise are rejected by selecting an appropriate trigger level for the discriminator. The arrival time of the photon pulses with respect to the LED excitation pulse are measured with a time to amplitude converter. A time to amplitude converter in principle is a stop watch. In the TAC a linear voltage ramp as a function of time is generated by charging a capacitor with a constant current source. This charging is started by a start pulse and stopped with an external stop pulse. The voltage of the capacitor which is proportional to the elapsed time between start and stop pulse is provided at an output of the TAC. In our case start and stop pulses are provided by the trigger pulse for the LED and the output of the discriminator. The reason for this is to detect the maximum amount of counts. Timing information is usually obtained by processing the output of the TAC with a pulse-height analyzer (PHA) [2]. Here, Ortec 567 TAC was used to obtain the decay profiles of the cerium emission.

Relaxation times of Ce were acquired as a function of temperature for two different Ce^{3+} concentrations, 0.1% and 3%. In the case of 0.1% Ce^{3+} the sample was excited near the center of the lowest absorption band at 470 nm and luminescence was detected near the peak of the emission band at 560 nm whereas for 3% Ce, the sample was excited at 540 nm and luminescence was detected at 710 nm in order to target the shifted Ce^{3+} sites. We note that no luminescence was observed when the low concentration sample was excited at 540 nm. The sample temperature was varied from 300 K to about 700 K. A thermocouple was used to measure the temperature of the sample accurately. Temperatures beyond 600 K were reached by using a conventional tube furnace instead of the optical furnace. In this case the sample was placed inside a quartz tube with an optical window to facilitate excitation and luminescence detection. The data acquisition duration at each temperature was typically 300 s. During the measurements the temperature was kept constant within temperature $\pm$

0.5 K. The decay time of the Ce luminescence at each temperature was obtained by fitting the data with a single exponential decay equation.

3.6 Experimental Results

Excitation and Emission spectra of YAG:Ce^{3+}

Excitation and emission spectra for YAG:Ce^{3+} is shown in Figure 3.4. The peak for excitation is about 470 nm and the peak for emission lies around 560 nm. Moreover, Figure 3.5 show the emission curves for 0.2 % YAG:Ce and 3 % YAG:Ce. It is clear from this that the high doped sample is a little red shifted.

When performing the lifetime measurements on the high concentration sample, an excitation wavelength of 540 nm was chosen as oppose to 470 nm in order to target the distortedCe^{3+} sites. At 540 nm the undistorted Ce sites (which are exclusive sites in the low concentration samples) cannot be excited. For the same reason the emission of high concentration YAG:Ce was detected at 710 nm.

Lifetime measurements of YAG:Ce^{3+}

Figure 3.6 shows the decay of luminescence of YAG doped with 3% Ce^{3+} at 300 K under 540 nm excitation and 710 nm detection. Similarly, Figure 3.7 shows the decay of luminescence of YAG doped with 0.1% Ce^{3+} at 300 K under 470 nm excitation and 560 nm detection. These curves show single exponential decays as expected and thus the data is fitted by a single exponential equation in order to find the corresponding total decay lifetime τ_T.

According to Figures 3.6 and 3.7 the luminescence lifetimes at room temperature(300 K), obtained by the single exponential fit for low and and high doped YAG:Ce samples are 63.6 ns and 72.3 ns respectively. This increase in room temperature luminescence lifetime at high concentration of YAG:Ce is discussed in the conclusions.

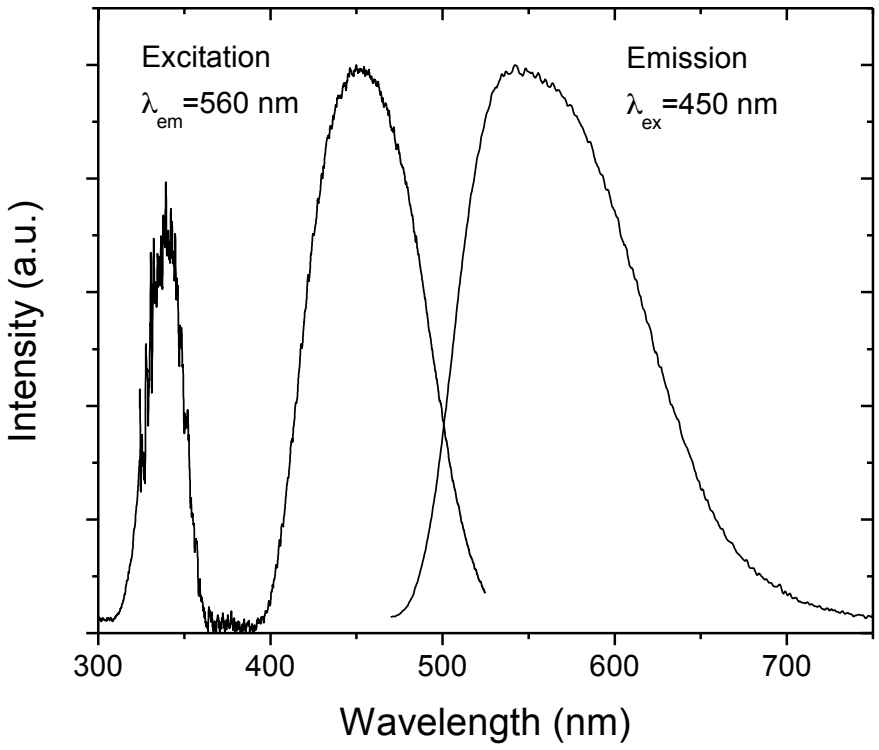

Figure 3.4: Excitation and emission spectra for YAG:Ce^{3+}

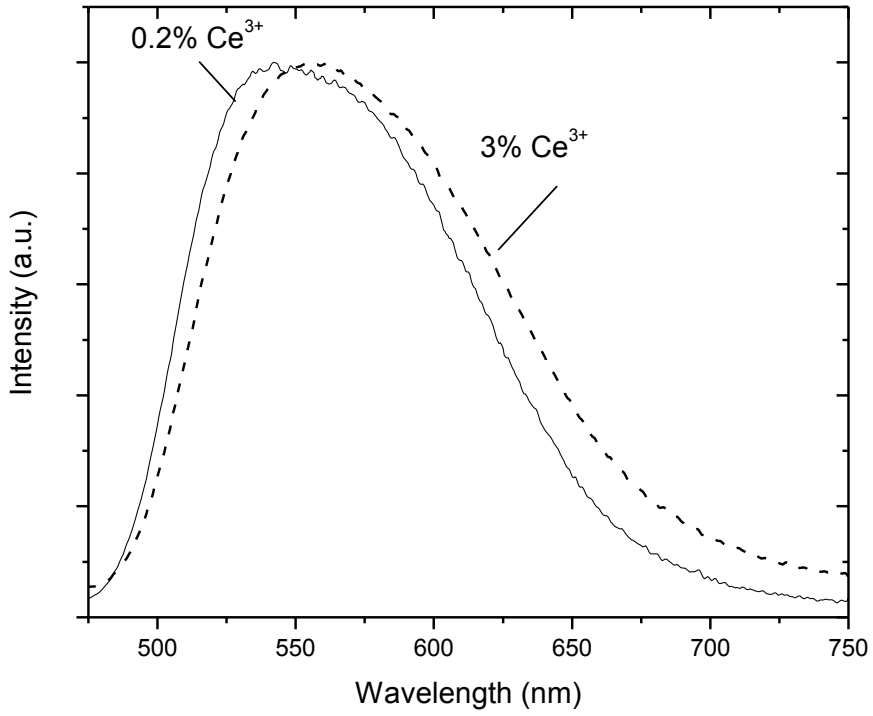

Figure 3.5: Emission spectra for 0.2 % and 3 % YAG:Ce^{3+} at room temperature.

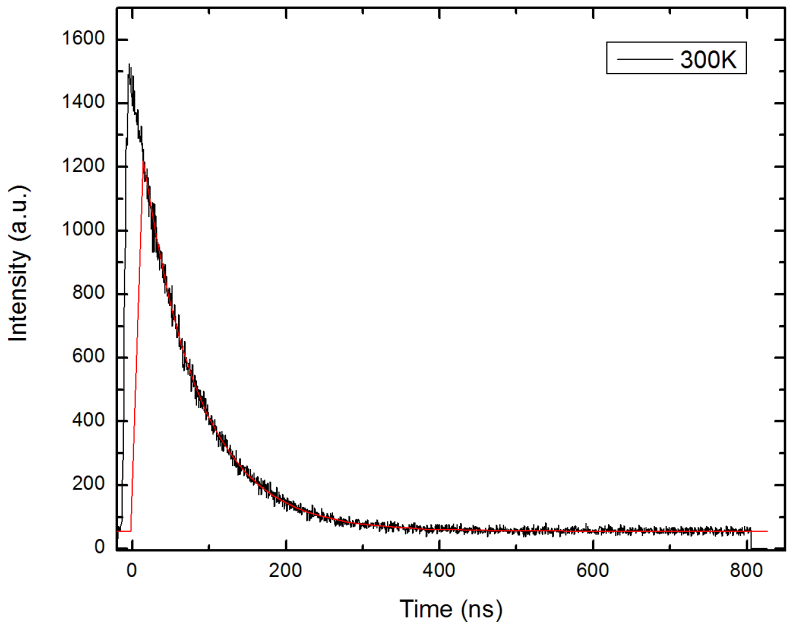

Figure 3.6: The decay curve of luminescence for YAG:Ce^{3+} 3% at 300 K. Excitation wavelength = 540 nm and detection wavelength = 710 nm. Here, $\tau_r = 72.3 \pm 0.3$ ns.

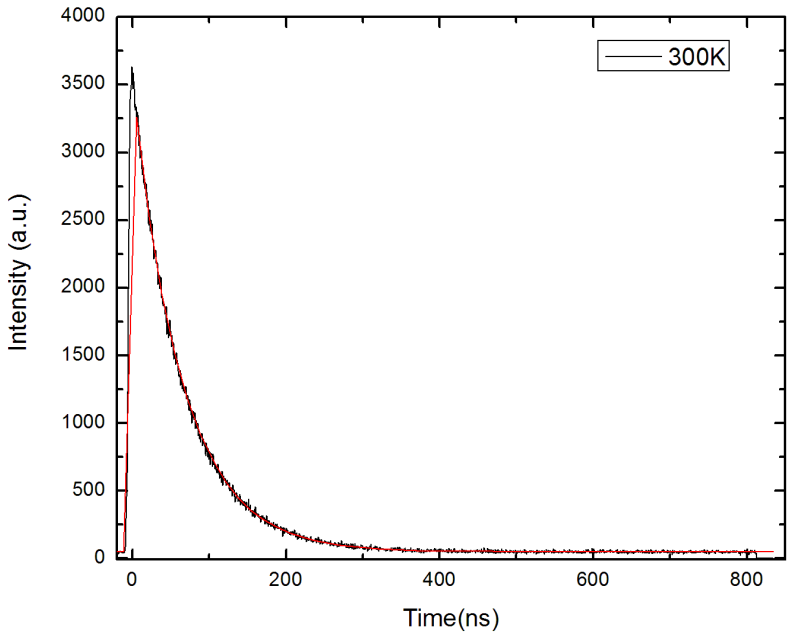

Figure 3.7: The decay curve of luminescence for YAG:Ce^{3+} 0.1% at 300 K. Excitation wavelength = 470 nm and detection wavelength = 560 nm. Here, $\tau_r = 63.6 \pm 0.1$ ns.

Luminescence lifetime measurements were carried out for several different temperature values in order to establish the behavior of the luminescence lifetime against temperature. We were able to go up to 650 K with the high concentration sample (3 % YAG:Ce) and were able to go up to 700 K in low concentration one. The reason that we cannot go beyond 650 K for the high concentration sample is as follows.

Figure 3.8 shows the decay curves for both YAG:Ce^{3+} 0.1% and 3% at 565 K. It is evident that the background signal at high concentration is significantly larger than that of the low concentration. Also from Figures 3.6 and 3.7 we can see that the detected intensities are low in high concentration Ce sample. This indicates that there are not many distorted Ce^{3+} sites in the sample. Moreover, in the case of high concentration we observe at a wavelength of 710 nm while in the case of low concentration, we observe at 560 nm. Therefore, when we reach very high temperatures, the signal at a detection wavelength of 710 nm are stronger affected by the high energy shoulder of the thermal background than signals recorded at 540 nm. This is further supported by Figure 3.9 which shows the decay curve for 3% Ce at very high temperature.Finally, since the high concentration sample has a lower quenching temperature than the low concentration one, data at extreme high temperatures were not vital for the interpretation of the quenching process. Due to all these reasons, the lifetime measurements on 3% Ce were carried out only up to 650 K.

Configurational Coordinate Model Analysis of Luminescence Lifetime:

Figure 3.10 shows the behavior of the luminescence lifetime against different temperatures for 3% Ce^{3+}. To investigate the luminescence quenching mechanism in 3% YAG:Ce, this

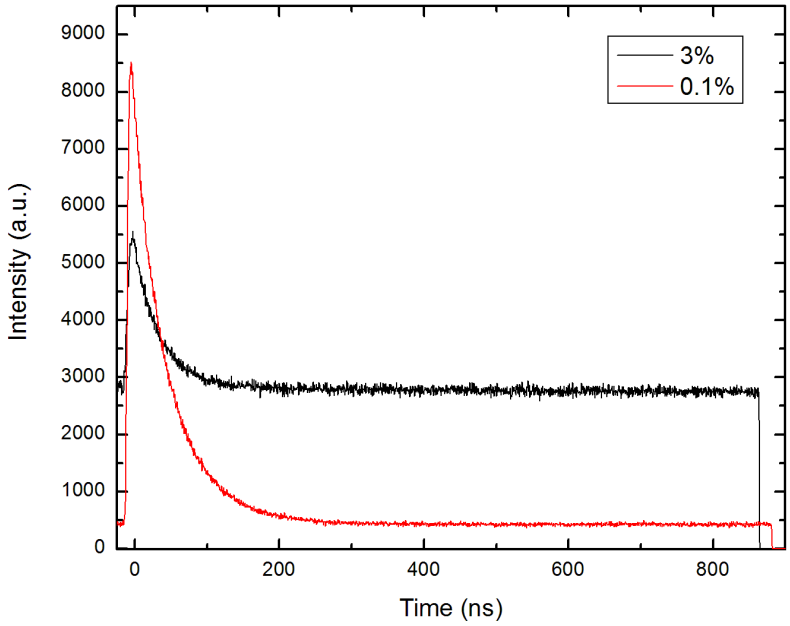

Figure 3.8: Comparison of luminescence decay curves for YAG:Ce^{3+} 3% and 0.1% at 565 K

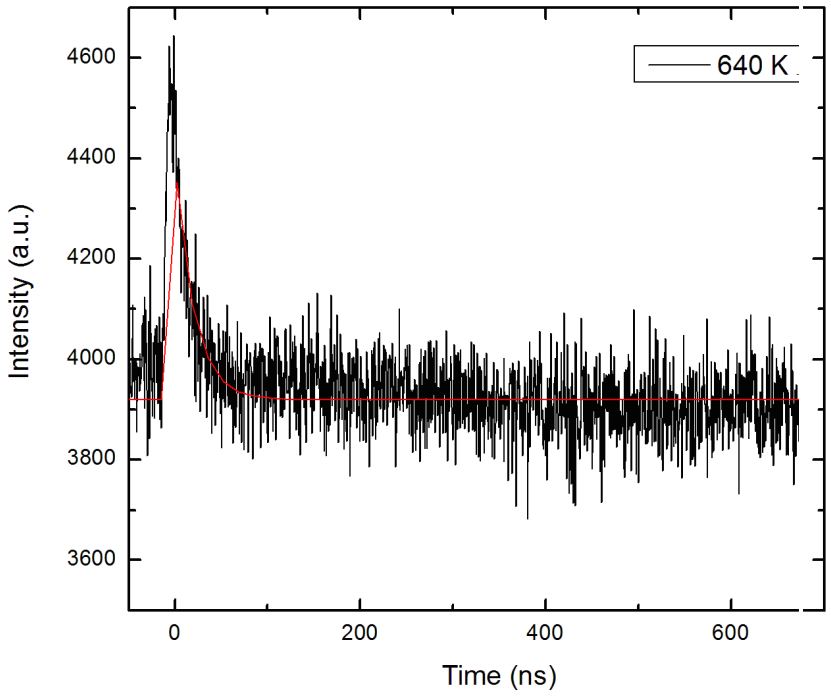

Figure 3.9: The decay curve of luminescence for YAG:Ce^{3+} 3% at 640 K. Excitation wavelength = 540 nm and detection wavelength = 710 nm. Here, $\tau_r = 20 \pm 1$ ns.

graph is fitted with "Arrhenius equation" given by;

$$\tau_T = \frac{1}{\frac{1}{\tau_r} + Be^{-\Delta E/kT}} \tag{3.5}$$

Where, ΔE - Activation energy, k - Boltzmann constant, T - Temperature in Kelvin and B - Attempt frequency. Moreover, $Be^{-\Delta E/kT}$ term represents the Γ_{nr} introduced in section 3.4.

It was found that at an excitation wavelength of 540 nm and 710 nm detection, YAG:Ce^{3+} 3% shows $\frac{1}{\tau_r} = 1.39 \times 10^7 s^{-1}$. The pre-factor $B = 4.70 \times 10^{11} s^{-1}$ with activation energy $\Delta E = 0.50$ eV. Here, the excitation wavelength 540 nm was chosen in order to target the disturbed Ce^{3+} sites as explained previously. Further, Figure 3.9 shows that the lifetime (τ_r = 72 ns) is independent of temperature up to about 400 K. The lifetime shortens rapidly as the temperature is raised beyond 400 K, indicating the onset of non-radiative transitions.

Figure 3.11 shows the temperature dependence of luminescence lifetime of 0.1% YAG:Ce^{3+}. Here, the 0.1% Ce sample is excited at 470 nm and detected at 550 nm which are the peaks of excitation and emission curves of YAG:Ce shown in Figure 3.4. We find the activation energy for low doped samples to be $\Delta E = 5192 cm^{-1} (0.64 eV)$ which is 0.14 eV larger than that of high-doped sample. The significance of these values are discussed in our conclusions section. Here, $\frac{1}{\tau_r} = 1.56 \times 10^7 s^{-1}$ with a pre-factor $B = 4.84 \times 10^{11} s^{-1}$ and the onset of the non-radiative transition is observed at about 450 K.

Figure 3.12 shows the lifetime measurements on both YAG:Ce 3% and 0.1% against temperature. It is evident from this data that in the high concentration sample Ce quench faster than in the low concentration one. Thus we observe low luminescence quenching temperatures in high doped sample as observed in other studies [11].

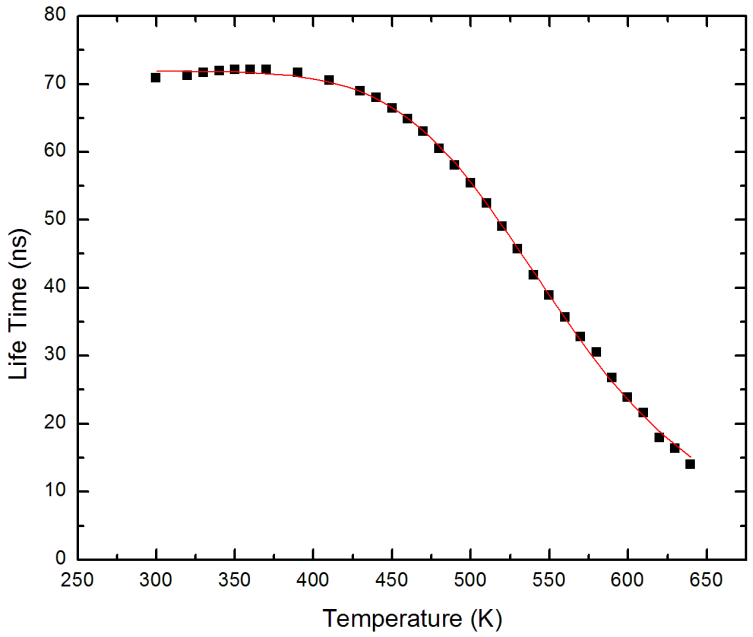

Figure 3.10: Luminescence lifetime measurements for YAG:Ce^{3+} 3% against temperature. The excitation wavelength is 540 nm. $\Delta E = 4045cm^{-1}(0.50eV)$.

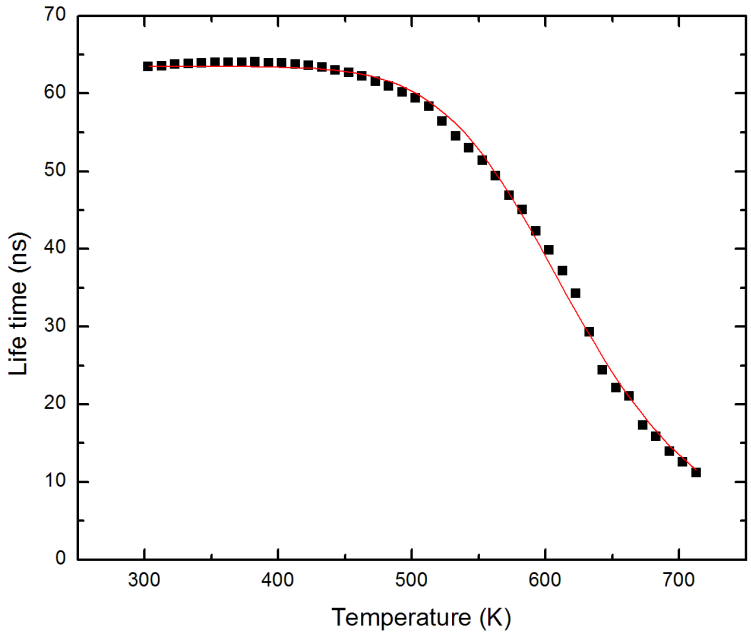

Figure 3.11: Luminescence lifetime measurements for YAG:Ce^{3+} 0.1% against temperature. The excitation wavelength is 470 nm. $\Delta E = 5192 cm^{-1}(0.64eV)$.

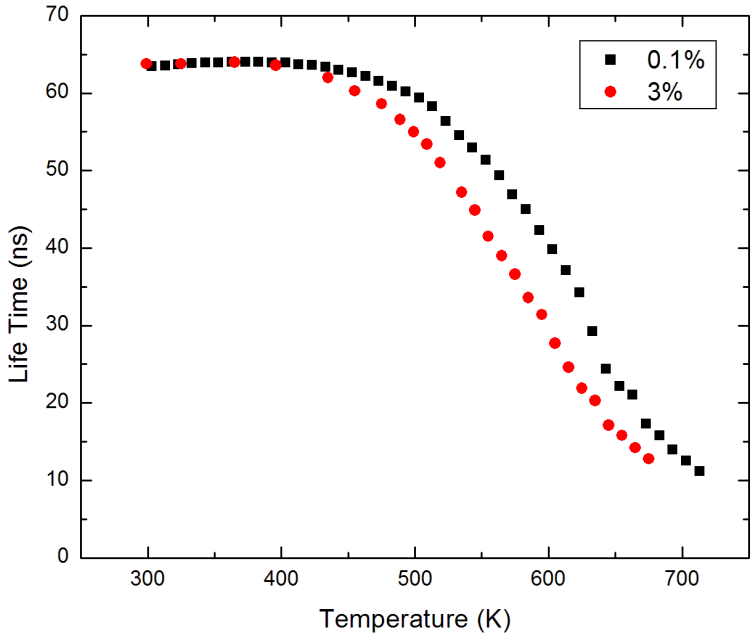

Figure 3.12: Luminescence lifetime measurements for YAG:Ce^{3+} 3% and 0.1% against temperature. The excitation wavelength for Ce^{3+} 3% is 540 nm, $\Delta E = 4045cm^{-1}(0.50eV)$. The excitation wavelength for Ce^{3+} 0.1% is 470 nm, $\Delta E = 5192cm^{-1}(0.64eV)$.

Single-frequency Phonon Model Analysis of Luminescence Lifetime:

Luminescence lifetime vs. temperature graphs for low and high concentration of Ce were fitted with the following equation which is obtained using a single-frequency phonon model (Equation 2.8 in section 2.3).

$$\tau_T = \frac{1}{\Gamma_r + \Gamma_{nr}(0)\left(1 - e^{-\frac{\hbar\omega_i}{kT}}\right)^{-p_i}} \tag{3.6}$$

Our results are summarized in Table 3.2. In this single-frequency phonon model, our calculated radiative lifetimes for 3 % and 0.1 % YAG:Ce at RT are 75 ns and 64 ns respectively. These lifetimes agree with our fitted values for the luminescence decay curves at RT (Figures 3.6 and 3.7).

Table 3.2: Fitted parameters for low and high concentration YAG:Ce

	0.1 % YAG:Ce	3 % YAG:Ce
Γ_r	$1.55 \times 10^7 s^{-1}$	$1.33 \times 10^7 s^{-1}$
$\Gamma_{nr}(0)$	$0.3 \times 10^5 s^{-1}$	$0.9 \times 10^5 s^{-1}$
p_i	29	28

Note: Γ_r - Radiative transition rate, $\Gamma_{nr}(0)$ - Non-radiative transition rate at T = 0 K and p_i - No. of phonons with energy $\hbar\omega_{eff} = 705.5$ cm^{-1}

Further, we find that an effective phonon energy of $\sim 706\ cm^{-1}$ is responsible for the non-radiative transition from $5d$ to $4f$ levels of Ce^{3+} in YAG:Ce. This effective phonon energy was selected by studying the vibronic spectrum of YAG [17] and also the best fit to our data.

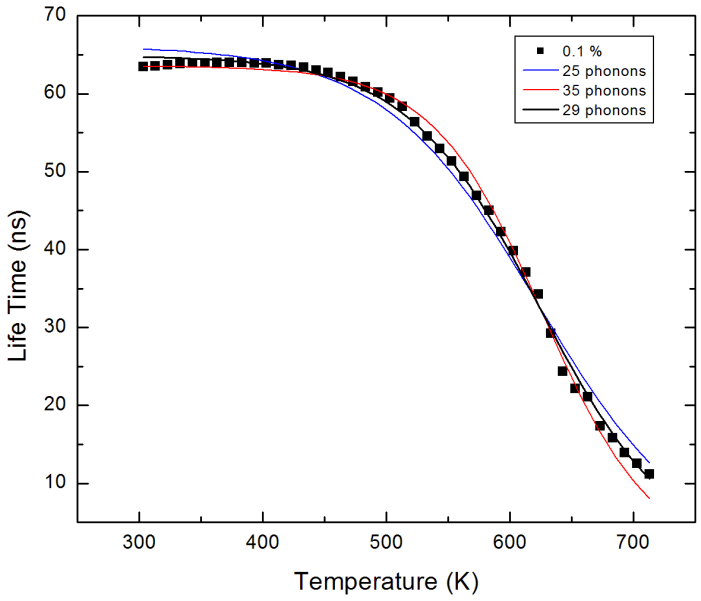

Figure 3.13: Best fit for luminescence lifetime measurements for 0.1 % YAG:Ce^{3+}.

When fitting the data for the low doped sample, the zero phonon energy of 20450 cm^{-1} [11] was used as the energy gap (ΔE) and thus the relationship between the effective phonon energy ($\hbar\omega_{eff}$) and the number of phonons (p_i) were kept constant, at ΔE ($p_i\hbar\omega_i = \Delta E$). Figure 3.13 show how the number of phonons p_i was optimized in order to obtain a good fit.

Studies carried out by Zverev *et.al.* on the temperature dependences of the probabilities of non-radiative transitions have shown that in the single frequency model approximation, the optical phonons with energy $\hbar\omega_{eff} \sim 700\ cm^{-1}$ play the predominant role in rare-earth doped YAG crystals [16]. Thus, our findings are comparable with the work by Zverev *et.al.*.

Figures 3.14 show the temperature dependence of the non-radiative transition rates Γ_{nr} for both 3 % and 0.1 % YAG:Ce samples. To calculate Γ_{nr}, it is necessary to know the probability of spontaneous non-radiative transitions $\Gamma_{nr}(0)$, the frequency (ω_i) and the number (p_i) of the optical vibrations involved in the transition. Our experimental values for $\Gamma_{nr}(0)$ and p_i are shown in Table 3.2. Further, our findings show an effective phonon energy of 706 cm^{-1} facilitating these non-radiative transitions. Thus, these values were used in order to calculate Γ_{nr} for each temperature.

Figures 3.14 show the onset of considerable non-radiative relaxation to be at about 400 K for high concentration sample and about 450 K for low concentration sample. Further, we observe a higher non-radiative decay rate for high concentration sample compared to the low concentration at a given temperature T.

Figure 3.15 shows the luminescence lifetimes for two YAG:Ce 3% samples. One is YAG:Ce provided by GE and the other is on the Meijerink groups YAG:Ce sample.

According to our studies, the luminescence lifetime of Meijerink sample and the sample provided to us by GE show the same lifetime at room temperature (72 ns). However, when the temperature is increased from RT, the Meijerink sample quenches almost immediately showing a very low quenching temperature.

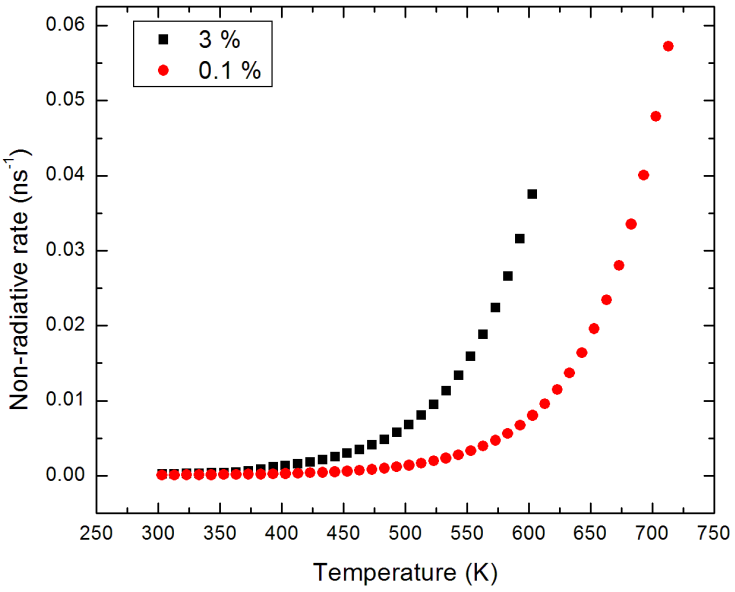

Figure 3.14: Temperature dependence of Γ_{nr} for 3 % and 0.1 % YAG:Ce. Here, Γ_{nr} values are calculated with $\hbar\omega_{eff} = 705.5$ cm^{-1} , $p_i = 29$ for 0.1 % and $p_i = 28$ for 3 % YAG:Ce.

The work done by Meijerink *et al.* suggest that the quenching mechanism of YAG:Ce is due to rapid energy migration among Ce ions and relaxation through some impurity site. Therefore, despite of the same Ce ion concentration in the two samples, the change in observed lifetimes could be due to the amount of impurities present in Meijerink sample. Thus, while we find that disturbed cerium sites ultimately cause increased thermal quenching in high concentration samples, the comparison of YAG samples nominally doped with the same cerium concentration can have different quenching behavior due to additional, unwanted impurities.

Comparing our results of the Meijerink sample with those obtained by Meijerink *et al.*, we find that our data show a more pronounced quenching. This may be in part due to the different excitation wavelength: The Meijerinkl group excite the sample at 406 nm and observe at 580 nm. However, in our studies, since we target mainly the disturbed sites, our excitation and detection wavelengths are 560 nm and 710 nm.

Another reason might be that the accuracy of the temperature measurements. In this experiment it is not easy to measure the temperature accurately. With previous experiences in experiments carried out on various phosphor materials at Happek lab, we believe that we have optimized the method of measuring temperature of our samples accurately.

Specifically, Meijerink et al. mount their samples onto a heating block which is in vacuum. It is reasonable to assume that at high heater block temperatures the sample temperature is actually lower than the reading of the thermometer, which is embedded in the heater block, suggests.

In our, more elaborate sample heater furnace, the sample is mounted on a support that is thermally insulated from the heater. The heater heats the sample indirectly through an exchange gas (nitrogen), as well as the thermocouple to monitor the exchange gas, and thus the sample temperature.

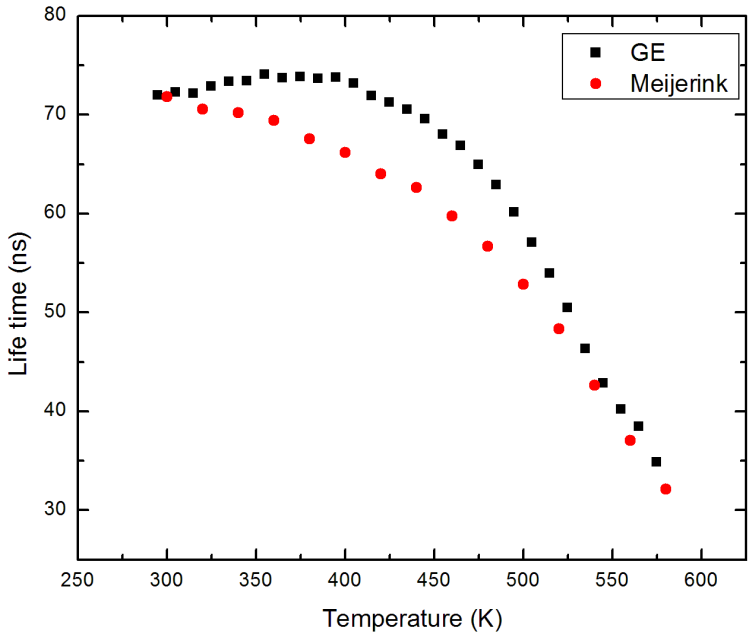

Figure 3.15: Luminescence lifetime measurements for YAG:Ce^{3+} 3% along with Meijerink results. Black - Happek lab results on YAG:Ce sample provided by GE and Red - Meijerink YAG:Ce sample. Here, $\lambda_{ex} = 540$ nm and $\lambda_{det} = 710$ nm.

3.7 Conclusions

The temperature dependence of luminescence quenching of Ce^{3+} in YAG:Ce was studied at high temperatures (>300 K). YAG:Ce samples of two different concentrations, 0.1% and 3% of Ce^{3+} were studied in order to better understand their quenching mechanisms. Excitation spectra showed a shift in the excitation energy with the increasing concentration of Ce^{3+}. Along with this shift in the excitation energy, a faster luminescence lifetime decay was observed.

According to Figures 3.6 and 3.7, at room temperature, a larger luminescence lifetime (72 ns) was observed for high concentration YAG:Ce compared to that of low concentration sample (64 ns). This is due to the fact that the radiative transition probability increases as the cube of the energy separation between the initial and final states [10]. Emission curves for low and high doped samples at room temperature (Figure 3.5) show a shift to larger wavelengths at higher concentrations which in tern result in a lower radiative transition rate for high doped sample at room temperature. This lowering of the radiative transition probability will finally result in a larger luminescence lifetime in high doped sample at RT.

We suggest that the quenching mechanism in high concentration YAG:Ce is due to level crossing in distorted sites of Ce^{3+}. When the Ce^{3+} ion is stimulated by light radiation, the electron at $4f$ ground state is promoted to the $5d$ excited state. There exist energy migration between Ce ions in the YAG crystal and the probability of this energy migration becomes larger with increased Ce concentration. The reason for this phenomena is that the reduction in ion-ion spacing with increasing dopant concentration. During this energy migration process, the energy may be transferred in to the distorted Ce sites and then luminescence quenching can occur through level crossing.

When the electron is at the excited state of the distorted Ce site, it returns to a lower vibrational level of the excited state by loosing the excessive energy to the surroundings.

After that, the electron may enter into high vibrational level of the ground state at the cross joint point shared by both the ground and excited states, continuously it relaxes into lower vibrational level of the ground state by releasing heat energy. This depopulation process via the crossing over process from excited state to ground state is addressed here as level crossing.

Figure 3.16 illustrates a configurational diagram summarizing our findings in the configurational coordinate model analysis of the luminescence lifetime. Here, the red curve is the excited $5d$ level for the disturbed Ce^{3+} sites and the $\Delta E = 0.50$ eV. We find that this energy level is shifted downward compared to that of the low concentration thus quenching faster.

Further analyses were carried out using a multi-phonon relaxation process using a single-frequency phonon model. At elevated temperatures, a decrease in Ce^{3+} $5d$ lifetimes was observed ($\sim$ 400 K for 3 % Ce and $\sim$ 450 K for 0.1 % Ce). Since YAG:Ce is known to have large energy gap between $5d$ and $4f$ levels, it is not surprising to have such high temperatures in order for the stimulated phonon process to compete with the radiative transition.

Non-radiative transition rate between the $5d$ and $4f$ levels of Ce^{3+} was studied and it was found that the number of phonons involved in the transition from $5d$ to $4f$ in low concentration sample ($p_i = 29$) requires more phonons compared to the high concentration sample ($p_i = 28$). That is, in the low concentration YAG:Ce, more phonons are needed since the energy gap between $5d$ and $4f$ for Ce^{3+} is larger compared to that of high concentration. This is further illustrated in Figure 3.17. Here, the solid lines represent the radiative transition probability and the dotted lines indicate the non-radiative transition probability. Since we find lower number of effective phonons in the case of high doped sample, it is safe to illustrate the energy gap ΔE to be smaller in the case of 3% YAG:Ce compared to that of 0.1%.

Moreover, we find that an effective phonon energy of $\sim$ 706 cm^{-1} is responsible for the non-radiative transition between excited state and the ground state of Ce^{3+}. Studies on the frequencies of optical oscillations for the YAG crystals show that in the phonon

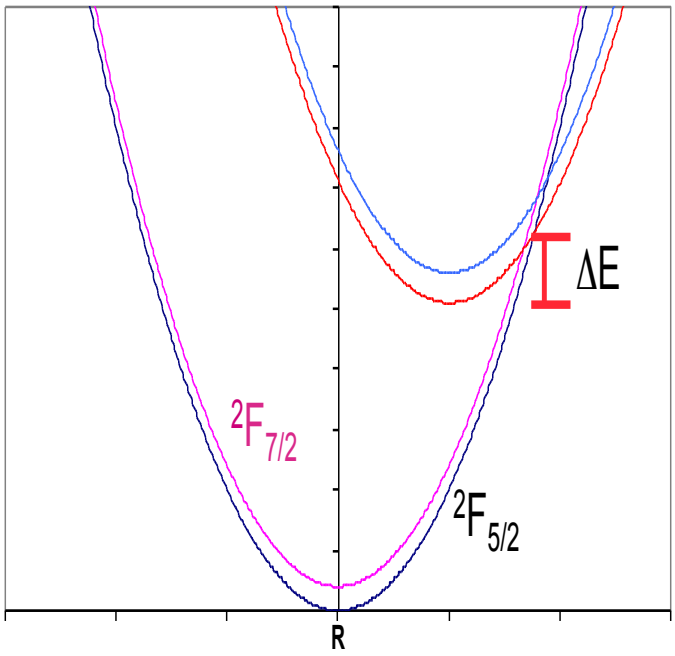

Figure 3.16: A sketch of the configurational diagram showing the excited states for high and low concentration Ce^{3+}.

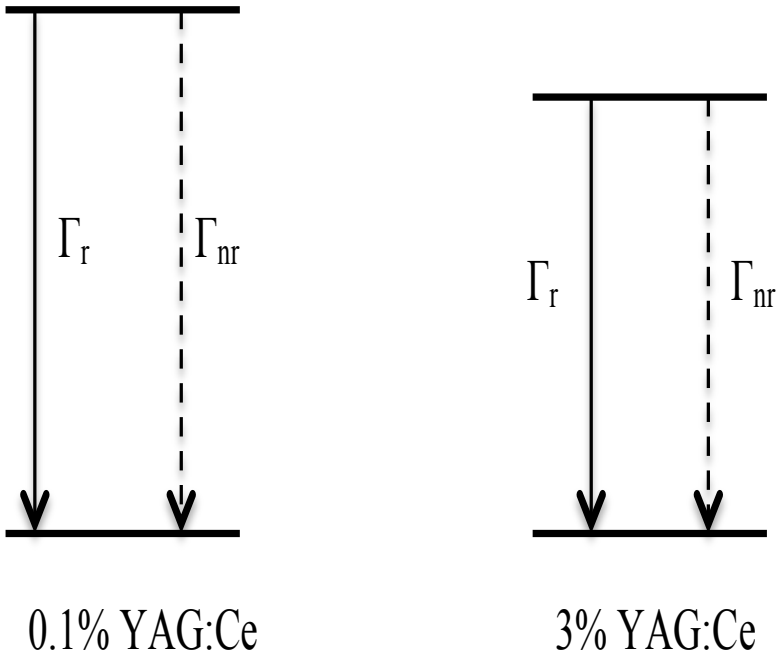

Figure 3.17: A sketch of the multi-phonon emission of low and high doped YAG:Ce^{3+}.

spectrum of the YAG, there is a whole series of optical vibrations with energies up to 860 cm^{-1} ($\hbar\omega_i^{max}$) [15]. However, investigations carried out by Zverev *et.al.* on the electron vibrational spectra of the ions Nd^{3+} and Er^{3+} in YAG crystals have shown that the intensity of the oscillations with frequencies 800 - 860 cm^{-1} is very low, whereas those with frequency $\sim$ 700 cm^{-1} are quite intense. Apparently, oscillations with frequencies 800 - 860 cm^{-1} are weakly coupled with the active rare-earth ion and exert no significant influence on the non-radiative transitions between the levels of the rare-earth ions in the YAG crystals [16]. Thus our result of $\hbar\omega_{eff} \sim 706\ cm^{-1}$ is comparable to these findings.

Finally, comparisons to studies carried out by Meijerink *et al.* were made. Meijerink *et al.* claim that the observed low quenching temperature in high concentration sample is due to energy migration from Ce ion to Ce ion and then quench through an impurity in the host material. However, we strongly suggest that in addition to this rapid energy migration, the observed low quenching temperature in high concentration YAG:Ce is due to level crossing.

Our results can also be generalized to other high concentration samples. While higher Ce concentration offer the advantage of a desired red-shifted emission spectrum, the disturbed cerium sites exhibit a reduced quenching temperature, hereby possibly limiting the use of phosphors with high cerium concentration in solid state lighting. These results are forthcoming in the Journal of Luminescence under "Non radiative processes in heavily doped $Y_3Al_5O_{12}$:Ce^{3+}" : M. Perera, A. A. Setlur and U. Happek.

References

[1] J. Garcia Sole, L.E. Bausa and D. Jaque, "An Introduction to the Optical Spectroscopy of Inorganic Solids".

[2] John H. Moore, Christopher C. Davis and Michael A. Coplan, "Building Scientific Apparatus. A practical guide to design and construction".

[3] Luis Seijo and Zoila Barandiaran, "4f and 5d Levels of Ce^{3+} in D_2 8-fold oxygen coordination" *Optical Materials 35 (2013) 1932-1940.*

[4] R. Kolesov, K.Xia, R. Reuter, R.Stohr, A.Zappe, J. Meijer, P.R. Hemmer and J. Wrachtrup, "Optical detection of a single rare-earth ion in a crystal" , *DOI: 10.1038/ncomms2034.*

[5] G. Blassse, A. Brill, J. Chem. Phys. 47 (1967) 5139.

[6] G. H. Dieke, "Spectra and Energy Levels of Rare Earth Ions in Crystals".

[7] R.R. Jacobs, W.F. Krupke, M.F. Weber, Measurement of excited-state-absorption loss for Ce^{3+} in $Y_3Al_5O_{12}$ and implications for tunable $5d$ to $4f$ rare-earth lasers. *Appl. Phys. Lett. 1978, 33, 410?412.*

[8] Y. Dong, G. Zhou, J. Xu, G. Zhao, F. Su, L. Su, G. Zhang, D. Zhang, H. Li, J. Si, Luminescence studies of Ce:YAG using vacuum ultraviolet synchrotron radiation. *Mater. Res. Bull. 2006, 41, 1959?1963.*

[9] C. Lei, L. Chun-Che, Y. Chiao-Wen, L. Ru-Shi , Light Converting Inorganic Phosphors for White Light-Emitting Diodes. *Materials 2010, 3(3), 2172-2195.*

[10] B. Henderson and G. F. Imbusch, "Optical spectroscopy of inorganic solids".

[11] V. Bachmann, C. Ronda, A. Meijerink, "Temperature quenching of yellow Ce^{3+} luminescence in YAG:Ce".

[12] M. Kucera, P. Hasa, J. Hakenova, "Optical and magneto-optical properties of Ce:YAG".

[13] G. Blasse, B.C. Grabmaier, Luminescent Materials, Springer, Berlin, 1994.

[14] Paolo Ghigna, Sonia Pin et.al. doi:10.1016/j.optmat.2011.07.015 "Local structure of the Ce^{3+} ion in the yellow emitting phosphor YAG:Ce".

[15] J. P. Hurrel, S. P. S. Porto, I. E. Chang, and S. S. Mitra, Phys. Rev., 173, 851 (1968).

[16] G. M. Zverev, G. Ya. Kolodnyi and A.M. Onishchenko; Zh. Eksp. Teor. Fiz. 60, 920-928 (March, 1971).

[17] Zhongli Wu, Baojiu Chen, Xiangping Li, Jinsu Zhang, Jiashi Sun, Hua Zhong, Hui Zheng, Lili Tong and Haiping Xia. "Optical transition properties, energy transfer mechanism and luminescent thermal stability of Sm^{3+} doped silicate glasses" Journal of Alloys and Compounds 663 (2016) 545e551.

Chapter 4

Luminescence of Ce^{3+} in Sodium Gadolinium Oxyborate

In Chapter 3, luminescence quenching mechanism of YAG:Ce is discussed in detail. Our results suggest that the lowering of the quenching temperature in high concentration samples of YAG:Ce is due to cerium ions in "distorted" sites. Further, in YAG:Ce, the luminescence quenching mechanism is identified as level crossing.

In this chapter, our work on Ce^{3+} doped sodium gadolinium oxyborate ($Na_2Gd_2O(BO_3)_2$; NABO) and the experimental results are discussed in detail. In this situation, Ce ions are known to occupy the Gd sites. According to Corbel *et.al.*, there are two distinct sites of Gd in NABO. Thus, Ce ions which occupy these two distinct sites are expected to have different luminescence quenching temperatures. The luminescence lifetimes of NABO:Ce at these two different sites are studied in order to understand their quenching mechanism.

4.1 Introduction

The comprehensive evaluations of the Ce^{3+} luminescence properties in various inorganic solids has shown that factors such as covalency, site coordination, symmetry, polarizability of the surrounding anions and network rigidity play an important role in determining the crystal field splitting and the centriod shift of the Ce^{3+} $5d$ state [1–5]. Studies of thermal quenching behavior of Ce^{3+} luminescence in the oxysulfate $Y_2O_2(SO_4)$ demonstrated that the efficiency of Ce^{3+} luminescence is generally low in solids, which offer free O^{2-} ion in the coordination sphere of the Ce^{3+} ion. It was suggested that the photoionization effect is responsible for the quenching of the Ce^{3+} luminescence in these materials.

The crystal structure and the luminescence of the Eu^{3+} ion in $Na_2Gd_2O(BO_3)_2$ has been reported by Corbel *et. al.* [6]. According to Corbel *et. al.* there are two crystallographically distinct sites for the rare earth ion, both with very low site symmetry of C_1 (Figure 4.1). Moreover, these rare earth ions are eight coordinated (GdO_8) and occupy the center of a distorted triangulated dodecahedra (bisdisphenoid).

Moreover, there are two free oxygen (labeled O(1) [6]), which are exclusively coordinated to the two rare earth ions. The free oxygen ion is slightly closer (or more tightly bound) to Gd(1) site relative to the Gd(2) site. The average $<$ Gd(1)-O$>$ and $<$ Gd(2)-O$>$ bond distances are 2.44 $\mathring{A}$ and 2.41 $\mathring{A}$, respectively. The two Na^+ ions occur in six and seven coordination, respectively. The borate groups occur as triangular BO_3^{3-} anion, which are isolated from each other.

The efficient interconfigurational ($4f^1 \leftrightarrow 5d$) emission transition of the Ce^{3+} ion in solids manifests as intense broad bands with fast decay due to their predominantly electric dipole character. In this dissertation the optical properties of the Ce^{3+} ion in the sodium gadolinium oxyborate $Na_2Gd_2O(BO_3)_2$ is examined as a function of temperature.

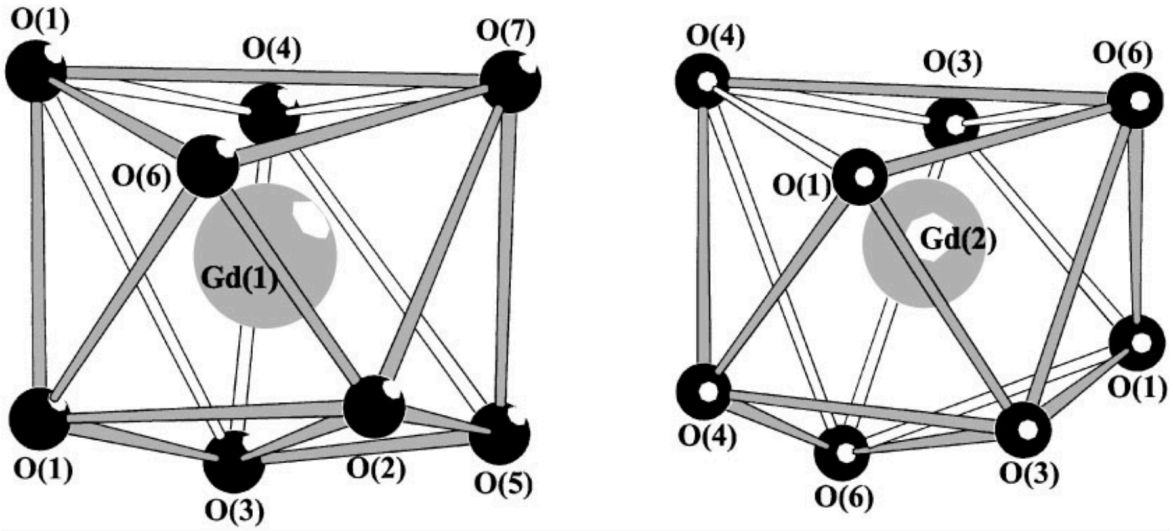

Figure 4.1: Rare earth polyhedra in $Na_2Gd_2O(BO_3)_2$ [6].

4.2 Experimental Setup

Excitation and Emission spectra

Excitation spectra were recorded in a modified Cary 14 spectrophotometer, using the chopped radiation of a deuterium lamp (UV) or tungsten lamp (VIS) as excitation source. The sample was placed into an Oxford Instruments flow-through cryostat, located in the sample chamber of the spectrophotometer. Luminescence was observed at right angles to the excitation with a Hamamatsu R212 photomultiplier tube (PMT), the detection wavelength was determined by narrow band interference filters. To increase the signal to noise ratio and to suppress the dark current of the PMT, the signal was processed with a Stanford lock-in amplifier. The excitation spectra were corrected for excitation photon flux using a calibrated Hamamatsu photodiode as reference detector.

Thermal quenching of Ce^{3+} lifetime in $Na_2Gd_2O(BO_3)_2$

The temperature dependence of the Ce^{3+} lifetime was measured under two different excitation wavelengths, 400 nm (Ce_A^{3+}) and 350 nm (Ce_B^{3+}). We find that there exist two different sites where Ce^{3+} ion can occupy in NABO and thus one quenches faster than the other. At room temperature, one site is almost completely quenched and therefore, measurements above room temperature involve only one site of Ce^{3+}. Here, we label the site where Ce ion sits above room temperature as "Site A" and below room temperature as "Site B". For site A, same experimental setup used in YAG:Ce experiment was used in order to measure the luminescence lifetimes. For site B, the sample was placed in the Oxford Instruments flow-through cryostat instead of the optical furnace and He gas is used to cool the sample in to low temperatures.

4.3 Experimental Results

Excitation and Emission Spectra

The excitation and emission spectra of $Na_2Gd_2O(BO_3)_2$:Ce at T= 10 K are shown in Figures 4.2 and 4.3, respectively. The broad excitation bands are assigned to electric-dipole allowed transitions from the Ce^{3+} ground state to crystal field split components of the $5d^1$ excited states. The sharp lines in the excitation spectrum are associated with optical transitions on the Gd^{3+} ion. This indicates efficient $Gd^{3+}\rightarrow Ce^{3+}$ energy transfer. This is not surprising in view of the favorable spectral overlap between the Ce^{3+} excitation bands and the excited states of the Gd^{3+} ion. Here, the $Ce^{3+}\rightarrow Gd^{3+}$ energy transfer is not possible since the relaxed excited state of the Ce^{3+} ion is located below the ^6P_J manifold of the Gd^{3+} ion.

The weak broad band near 200 nm corresponds to optical absorption edge of the host lattice. The low energy optical absorption edge appears to be typical for materials with free oxygen ions [7].

The emission spectrum is found to be strongly dependent on the excitation wavelength (Figure 4.3). When exciting into the lowest energy 5d band at 390 nm, the emission spectrum exhibits a clear doublet. The doublet nature of the emission band, which is characteristic of the Ce^{3+} emission, is attributed to the emission from the lowest energy 5d state to the two sublevels $^2F_{5/2}$ and $^2F_{7/2}$, split by spin-orbit coupling. This emission spectrum was converted to energy scale and decomposed into a sum of Gaussian bands. The calculated curves resulted in peaks at 2.76 eV (449 nm) and 2.54 eV (488 nm), respectively. The energy separation of 0.22 eV is in close correspondence with that observed for other Ce^{3+} activated materials [8]. This Ce^{3+} center, which is excitable with 400 nm radiation, is labeled as Ce_A^{3+} center.

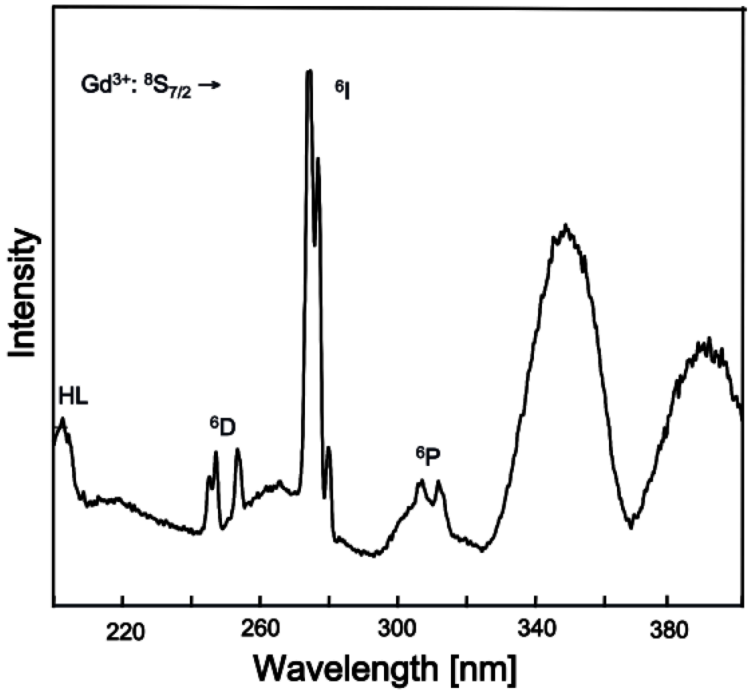

Figure 4.2: The excitation spectrum of NABO:Ce^{3+} at T= 10 K (λ_{em} = 380 nm). HL denotes host lattice absorption.

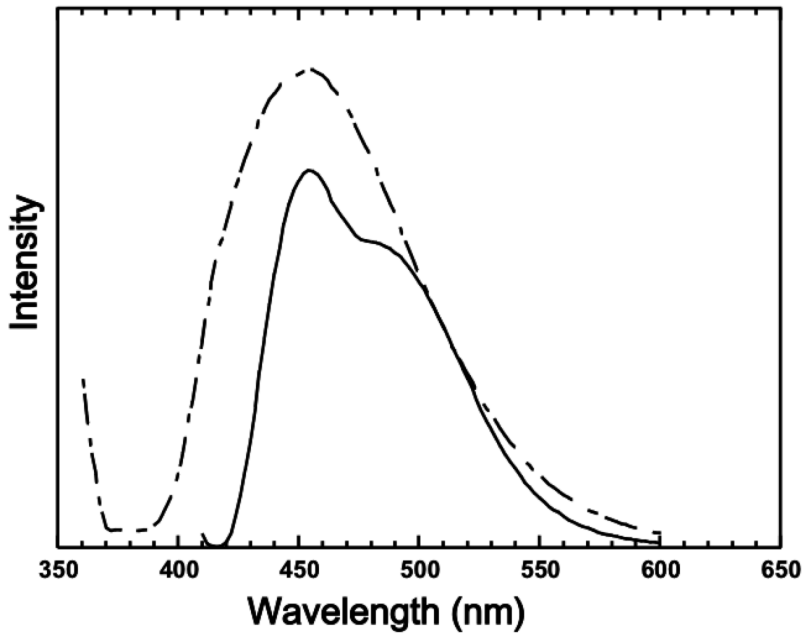

Figure 4.3: The emission spectra of NABO:Ce^{3+} at T= 10 K for $\lambda_{ex} = 390$ nm (solid curve) and $\lambda_{ex} = 350$ nm (dashed curve).

The ground state spin-orbit splitting of Ce^{3+} is not clearly resolved when exciting into the higher energy excitation band located at 350 nm. Instead, an inhomogeneously broadened emission band peaking near 450 nm is observed (Figure 4.3). Decomposing the emission spectrum into a sum of Gaussians resulted in two peaks centered at 2.82 eV (439 nm) and 2.61 eV (475 nm). This yields an energy separation of 0.21 eV. This Ce^{3+} center that is excitable with 350 nm UV radiation is labeled as Ce_B^{3+}.

In summary, the high energy excitation band at 350 nm is associated predominately with the Ce_B^{3+} center and the low energy excitation band at 400 nm is associated predominately with the Ce_A^{3+} center.

Thermal quenching of the Ce^{3+} lifetime

The excitation wavelengths for two sites where Ce^{3+} could occupy were identified as 400 nm and 350 nm respectively. Figure 4.4 and 4.5 shows the decay curve for NABO:Ce_A^{3+} at 300 K and the lifetime vs. temperature curve respectively.

It was found, using an Arrhenious fit that at an excitation wavelength of 400 nm and 450 nm detection, $Na_2Gd_2O(BO_3)_2$:Ce^{3+} shows $\frac{1}{\tau_r} = 1.99 \times 10^7 s^{-1}$ with activation energy $\Delta E =$ 0.49 eV. Further, it was found that the lifetime ($\tau_r = 48$ ns) is independent of temperature up to about 300 K. This short lifetime is typical of the spin and parity allowed transitions on the Ce^{3+} ion. The lifetime shortens rapidly as the temperature is raised beyond 300 K, indicating the onset of non-radiative transitions.

Figure 4.6 shows our findings on thermal quenching of lifetime on NABO:Ce_B^{3+} obtained for excitation at 350 nm. It was found that at 350 nm excitation, $Na_2Gd_2O(BO_3)_2$:Ce^{3+} shows $\frac{1}{\tau_r} = 2.3 \times 10^7 s^{-1}$ with activation energy $\Delta E = 0.08$ eV. Further, it was found that the lifetime ($\tau_r = 43$ ns) is independent of temperature up to about 70 K.

We have argued that the photoionization process is the most likely process, which quenches the Ce^{3+} luminescence in this material. Two possible reasons can be given in favor of the

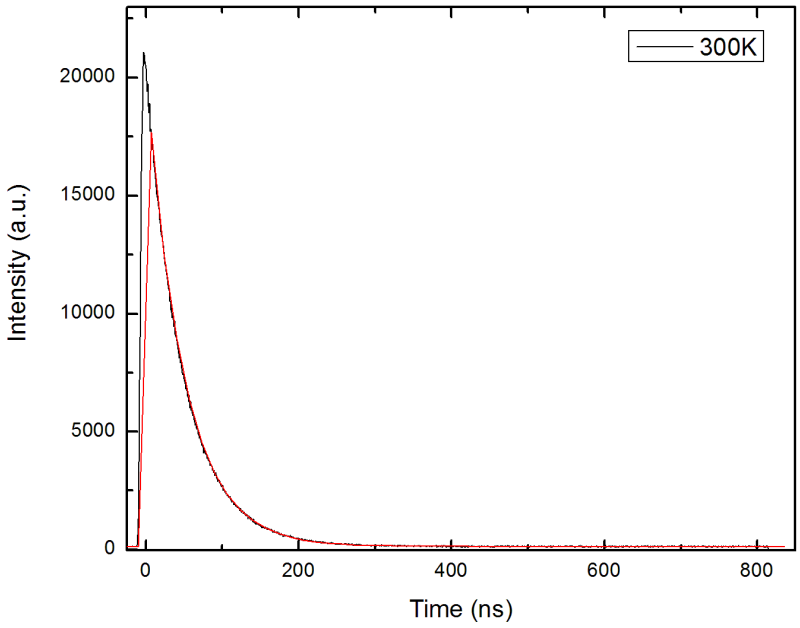

Figure 4.4: The decay curve of luminescence for $Na_2Gd_2O(BO_3)_2$ doped with Ce^{3+} at 300 K (site A). Excitation wavelength is 400 nm and detection at 450 nm.

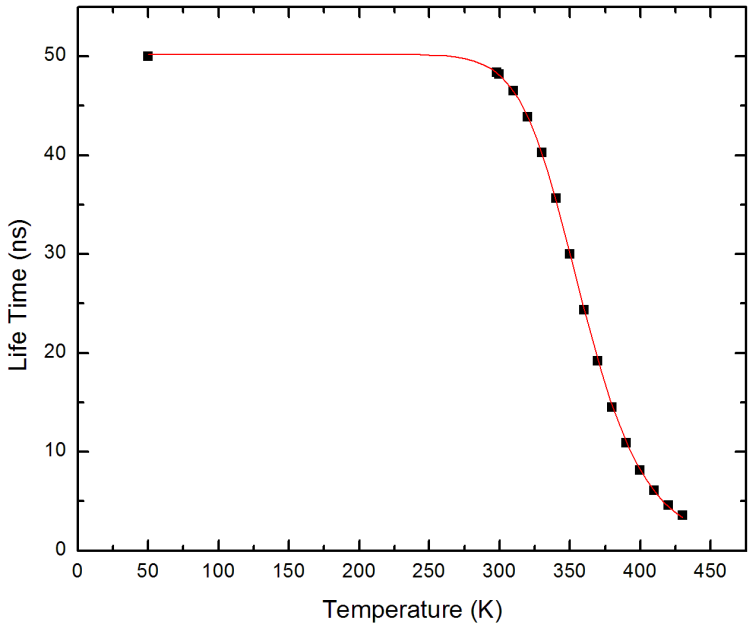

Figure 4.5: Thermal quenching of Ce^{3+} lifetime in $Na_2Gd_2O(BO_3)_2$ (site A - above room temperature). Excitation wavelength is 400 nm and detection at 450 nm.

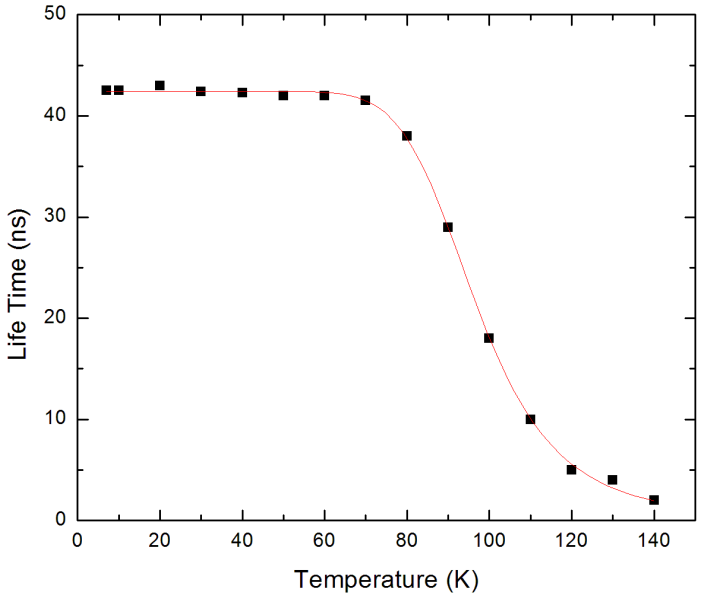

Figure 4.6: Thermal quenching of Ce^{3+} lifetime in $Na_2Gd_2O(BO_3)_2$ (site B - low temperature). Excitation wavelength is 350 nm.

photoionization process. First, the optical absorption edge of oxy compounds, in general, occurs at relatively low energy (200 nm- 220 nm) [9]. In $Na_2Gd_2O(BO_3)_2$ the host lattice optical absorption band is observed at about 200 nm. Second, the presence of free oxygen ions with high polarizability in the first coordination sphere of the Ce^{3+} ion can induce a strong negative potential at the Ce^{3+} site. This negative potential is known to raise the energy of the 4f 5d state of ions such as Sm^{2+} in materials with the fluorite structure [10] [11]. This can be attributed to the Madelung potential discussed in Chapter 2. Since there are two sites (Ce_A^{3+} and Ce_B^{3+}) with different Ce - O average distances, the site with higher number of O^{2-} ions is expected to yield a higher Madelung potential.

The combined effect of the lowering of the optical absorption energy of the host lattice and the raising of the 5d level energy can bring the 5d states in close proximity to the conduction band edge. This increases the probability of thermal quenching via the photoionization process. Hence, the activation energy represents the thermal energy required to promote an electron from the lowest excited state of the Ce^{3+} ion to the host lattice conduction band.

The decay curves of the Ce_B^{3+} center were single exponential at all temperatures and thus there is no evidence for energy transfer from this center to the Ce_A^{3+} center. Further, the quenching temperature of the center did not change when the Ce^{3+} concentration was increased to 0.5%. Therefore, we associate the strong luminescence quenching of this center with photoionization, which suggests that the 5d orbitals are energetically closer to the host lattice conduction band relative to the 5d orbitals of the Ce_A^{3+} center.

The Madelung potentials for the two sites of Ce in $Na_2Gd_2O(BO_3)_2$ were calculated using their "nearest neighbors". These were found to be 11.80 V and 11.95 V for $<$ Gd(1)-O$>$ = 2.44 $\mathring{A}$ and $<$ Gd(2)-O$>$ = 2.41 $\mathring{A}$ respectively. However, in order to get the exact value one would need to do the calculations according to Madelung.

4.4 Conclusions

The relaxation rate of Ce^{3+} ion in $Na_2Gd_2O(BO_3)_2$ has been investigated in the 10 K - 450 K temperature region. The optical properties of the Ce^{3+} ion in this host give evidence of two different Ce^{3+} sites, which is in accordance with the host lattice crystal structure. Here, doped Ce atoms occupy two distinct Gd sites resulting in different luminescence quenching temperatures. One site was found to be luminescent above room temperature (we call it site A: Ce_A^{3+}), while the others completely quenched at room temperature (site B: Ce_B^{3+}).

The excitation spectrum of $Na_2Gd_2O(BO_3)_2$:Ce show sharp lines along with broad excitation bands which correspond to the transitions from the Ce^{3+} ground state to crystal field split components of the $5d^1$ excited states. Here, these sharp lines are identified to be associated with optical transitions on the Gd^{3+} ion. Therefore, we observe efficient $Gd^{3+} \rightarrow Ce^{3+}$ energy transfer.

The luminescence intensity for site A, starts to quench very rapidly above room temperature and approaches values close to zero at about 400 K. The luminescence quenching of the other Ce^{3+} center occurs at relatively low temperature (70 K). Thus the onset of the non-radiative transition is $\sim$400 K and $\sim$70 K for site A and site B respectively. Also it is important to note that luminescence lifetime of site B at 140 K is about 2 ns. That is, Ce_B^{3+} centers quenches almost completely before the temperature at which Ce_A^{3+} centers start to quench. Table 4.1 summarizes the fitted values for the two sites A and B.

Table 4.1: Summary of results

	Site A - NABO:Ce_A^{3+}	Site B - NABO:Ce_B^{3+}
Γ_r	$1.99 \times 10^7 s^{-1}$	$2.33 \times 10^7 s^{-1}$
Δ E	0.49 eV	0.08 eV

Note: Γ_r - Radiative transition rate, Δ E - Activation energy

Here, note that the radiative transition rate (Γ_r) for site A is smaller than that of site B. This can be an indication that the energy gap between the excited $5d$ orbitals and $4f$ ground orbitals is larger in the case of Ce_B^{3+} center thus bringing it closer to the conduction band of the host. We attribute the quenching mechanism of Ce^{3+} lifetime and emission intensity in NABO:Ce to photoionization due to several reasons. Studies by Blasse *et.al.* suggest that eventhough the Ce^{3+} ion may be expected to luminesce in surroundings which have optical absorption far in the ultraviolet, if this optical absorption shifts to lower energies, quenching by photoionization becomes a competing process which rapidly eliminates the luminescence [9]. It was found that the host lattice optical absorption band in $Na_2Gd_2O(BO_3)_2$ is at about 200 nm (Figure 4.2). Therefore, NABO:Ce luminescence quenching also can be associated with photoionization.

Moreover, the presence of free oxygen ions with high polarizability in the first coordination sphere of the Ce^{3+} ion can induce a strong negative potential at the Ce^{3+} sites. Since site A and B has different Ce-O distances [6], this will bring the relaxed excited state of Ce^{3+} high up closer to the conduction band. This also makes us to conclude that the luminescence quenching by photoionization is more favourable in the case of NABO:Ce. Figure 4.7 illustrates the quenching through photoionization. Here, ΔE corresponds to the energy required to promote an electron from the relaxed excited state of the host lattice conduction band.. The fitted values shown in Table 4.1 for the two different sites Ce_A^{3+} and Ce_B^{3+} indicate that this gap for Ce_B^{3+} center is smaller than that of Ce_A^{3+}.

The above mentioned results along with the Madelung calculations considering "all" surrounding neighbors of the two Ce^{3+} cites are forthcoming in the Journal of Optical Materials under "Site Specific Relaxation Dynamics of Ce^{3+} in $Na_2Gd_2O(BO_3)_2$" : M. Perera, A. A. Setlur and U. Happek.

NABO:Ce has an interesting feature where Ce^{3+} can occupy two distinct sites in the crystal. We find that Ce_B^{3+} centers) are almost fully quenched by the quenching of Ce_A^{3+}

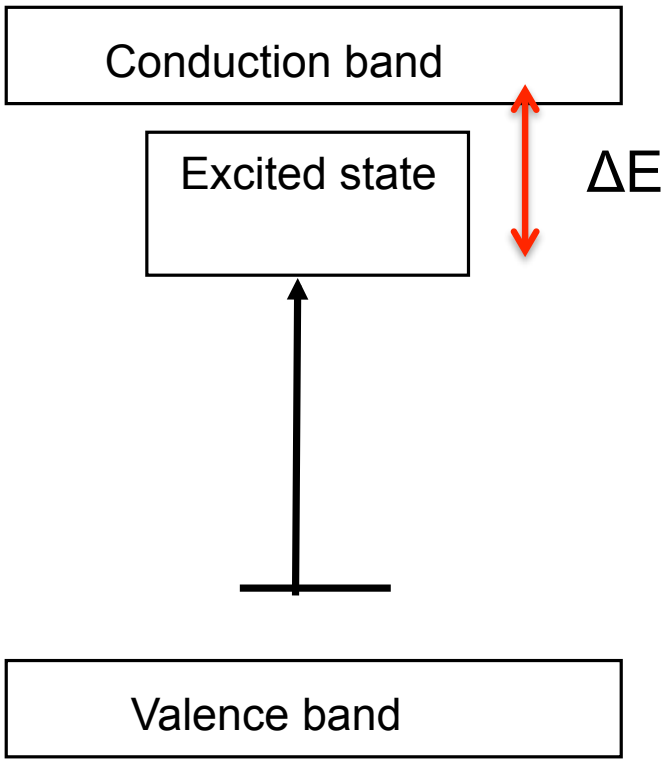

Figure 4.7: Schematic diagram showing the thermal quenching mechanism of Ce^{3+} in $Na_2Gd_2O(BO_3)_2$.

centers begin. However, the quenching temperatures associated with both of these Ce^{3+} centers are considerably low compared to YAG:Ce. This explains the wide commercial use of YAG:Ce. Further, the level crossing luminescence quenching mechanism in YAG:Ce makes them more stable compared to NABO:Ce where photoionization occurs.

References

[1] P. Dorenbos, J. Lumin., 91 (2000) 155.

[2] P. Dorenbos, Phys. Rev. B 62, (2000)15640.

[3] P. Dorenbos, Phys. Rev. B 62, (2000)15650.

[4] P. Dorenbos, Phys. Rev. B 64, (2001) 125117.

[5] P. Dorenbos, Phys. Rev. B 65 (2002) 235110.

[6] C. Corbel, M. Leblanc, E. Anti-Fidancev and M. Lemaitre-Blaise, J. Solid. St. Chem., 144 (1999) 35.

[7] G. Blasse and G. J. Dirksen J. Electrochem. Soc. 136 (1989), p. 1550.

[8] N. Kodama, M. Yamaga and B. Henderson, J. Phys.:Condens. Matter 8 (1996) 3505.

[9] G. Blasse, W. Schipper and J. J. Hamelink Inorg. Chem. Acta 189 (1991) 77.

[10] W. Mou and D. S. McClure, Phys. Rev. B 47 (1993) 11031.

[11] L. L. Chase, S. A. Payne and G. D. Wilke J. Phys. C 20 (1986) 953.

Chapter 5

Outlook

In this dissertation, the relaxation dynamics of trivalent cerium ions and their quenching mechanisms for $Y_3Al_5O_{12}$:Ce^{3+} and $Na_2Gd_2O(BO_3)_2$:Ce^{3+} are discussed in detail. This chapter focusses on our future work to be done with $Na_2Gd_2O(BO_3)_2$:Ce^{3+}.

The evaluation of the spectroscopic properties of the Ce^{3+} ion in $Na_2Gd_2O(BO_3)_2$ (NABO) show the presence of two emitting centers (we called them sites A and B). The luminescence intensity for site A, starts to quench very rapidly above room temperature and approaches values close to zero at about 400 K. The luminescence quenching of the other Ce^{3+} center occurs at relatively low temperature (70 K). In both cases, photoionization of the Ce^{3+} centers is held responsible for the luminescence quenching.

Madelung potentials stated in Chapter 4 are considering only the nearest neighbors of the two different Ce^{3+} centers in NABO. However, the problem remains to explain the differences between the behaviors of the two centers in a more precise quantitative manner. For this reason Madelung calculations are to be performed in order to find the energy levels within the band gap. Corbel *et.al.* have performed the structure determination of $Na_2Gd_2O(BO_3)_2$. The starting set of atomic coordinates was obtained from the analysis of the Patterson map [1]. The Table 5.1 gives atomic coordinates of $Na_2Gd_2O(BO_3)_2$.

Table 5.1: Table showing atomic coordinates in $Na_2Gd_2O(BO_3)_2$. Table taken from "Crystal Structure of $Na_2Gd_2O(BO_3)_2$ (Ln = Sm, Eu and Gd) and Optical Analysis of $Na_2Gd_2O(BO_3)_2$:Eu^{3+} " [1]

Atom	Site	x	y	z
Gd(1)	4e	0.18531(3)	0.08225(5)	0.08949(3)
Gd(2)	4e	0.98249(3)	0.45948(5)	0.18103(3)
Na(1)	4e	0.5229(3)	− 0.0573(5)	0.2624(4)
Na(2)	4e	0.6094(4)	0.2622(7)	0.0469(4)
O(1)	4e	0.9728(5)	0.1235(8)	0.0959(5)
O(2)	4e	0.3179(5)	− 0.2556(8)	0.1359(6)
O(3)	4e	0.1700(5)	0.2621(8)	0.3645(5)
O(4)	4e	0.1504(5)	0.4594(8)	0.0877(6)
O(5)	4e	0.3980(5)	0.162(1)	0.0552(5)
O(6)	4e	0.8486(5)	0.2581(8)	0.2716(5)
O(7)	4e	0.3727(6)	0.149(1)	0.3401(6)
B(1)	4e	0.3183(7)	0.251(1)	− 0.0797(7)
B(2)	4e	0.2097(7)	− 0.347(1)	0.1496(8)

It is in our future work to calculate the Madelung potential using these findings from Corbel *et.al.* and prove our findings on luminescence quenching of Ce^{3+} ion in $Na_2Gd_2O(BO_3)_2$. Basically, in order to support our findings, the Madelung potential of site B should be larger than that of site A. If that is the case, site B excited state is more closer to the conduction band of the host lattice and therefore will yield a lower activation energy Δ E compared to site A as observed experimentally. Figure 5.1 is an illustration of our expectations upon Madelung calculations. In this figure, the blue arrow indicates the ionization of free Ce^{3+} ion while E_{PI} indicate the ionization energies of the two sites. Here, the photoionization energy depends on ionization potential of free ion, location of the conduction band, Madelung potential V_M at each luminescent center.

Madelung potential at a certain site can be calculated with equation 5.1. Here, $V_{M(i)}$ is the Madelung potential at site i, q_j is the charge of atom j and r_{ij} represents the average distance from the atom i to the j^{th} atom.

$$V_{M(i)} = \sum_i \frac{1}{4\pi\epsilon_0} \frac{q_j}{r_{ij}} \tag{5.1}$$

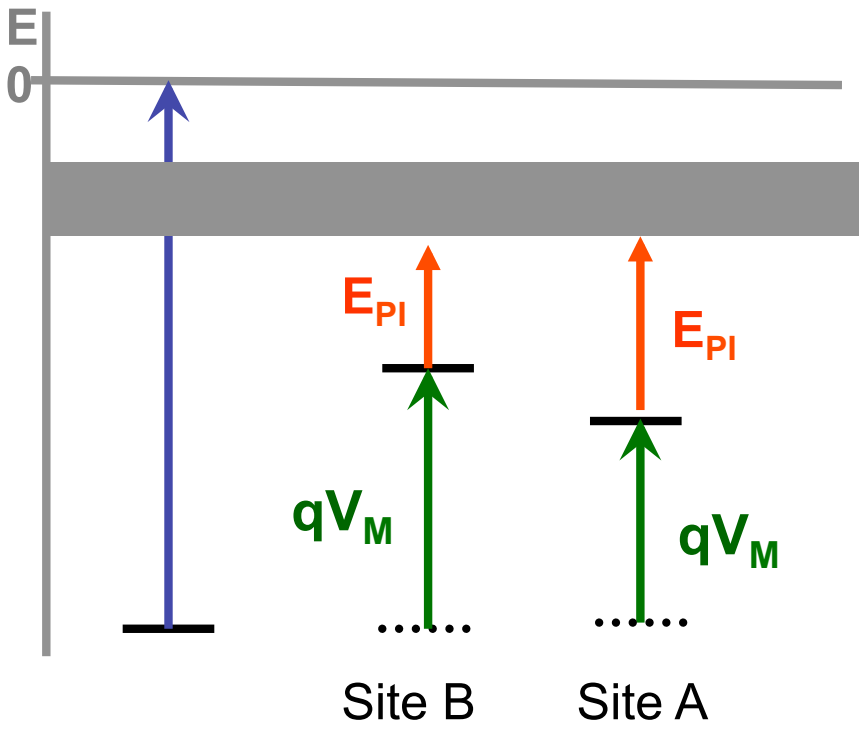

Figure 5.1: Madelung potential calculations on NABO:Ce.

References

[1] C. Corbel, M. Leblanc, E. Anti-Fidancev and M. Lematre-Blaise, J. Solid. St. Chem., 144 (1999) 35.